Monthly Notices of the ROYAL ASTRONOMICAL SOCIETY

MNRAS **497,** 389–404 (2020)
Advance Access publication 2020 July 16

doi:10.1093/mnras/staa1937

Inverse stellar population age gradients of post-starburst galaxies at $z = 0.8$ with LEGA-C

Francesco D'Eugenio [1]★ Arjen van der Wel,[1,2] Po-Feng Wu (吴柏锋),[2,3] Tania M. Barone [4,5,6] Josha van Houdt,[2] Rachel Bezanson,[7] Caroline M. S. Straatman,[1] Camilla Pacifici,[8] Adam Muzzin,[9] Anna Gallazzi,[10] Vivienne Wild [11] David Sobral,[12] Eric F. Bell,[13] Stefano Zibetti [10] Lamiya Mowla[14] and Marijn Franx[15]

[1]*Sterrenkundig Observatorium, Universiteit Gent, Krijgslaan 281 S9, B-9000 Gent, Belgium*
[2]*Max-Planck-Institut für Astronomie, Königstuhl 17, D-69117 Heidelberg, Germany*
[3]*National Astronomical Observatory of Japan, 2-21-1 Osawa, Mitaka, Tokyo 181-8588, Japan*
[4]*Research School of Astronomy and Astrophysics, Australian National University, Canberra, ACT 2611, Australia*
[5]*Sydney Institute for Astronomy, School of Physics, The University of Sydney, Sydney, NSW 2006, Australia*
[6]*ARC Centre of Excellence for All Sky Astrophysics in 3 Dimensions (ASTRO 3D), Australia*
[7]*Department of Physics and Astronomy and PITT PACC, University of Pittsburgh, Pittsburgh, PA 15260, USA*
[8]*Space Telescope Science Institute, 3700 San Martin Drive, Baltimore, MD 21218, USA*
[9]*Department of Physics and Astronomy, York University, 4700 Keele St, Toronto, ON M3J 1P3, Canada*
[10]*INAF-Osservatorio Astrofisico di Arcetri, Largo Enrico Fermi 5, I-50125 Firenze, Italy*
[11]*School of Physics and Astronomy, University of St Andrews, North Haugh, St Andrews KY16 9SS, UK*
[12]*Department of Physics, Lancaster University, Lancaster LA1 4YB, UK*
[13]*Department of Astronomy, University of Michigan, Ann Arbor, MI 48109, USA*
[14]*Astronomy Department, Yale University, New Haven, CT 06511, USA*
[15]*Leiden Observatory, PO Box 9513, NL-2300 RA Leiden, the Netherlands*

Accepted 2020 June 28. Received 2020 June 23; in original form 2020 March 25

ABSTRACT

We use deep, spatially resolved spectroscopy from the Large Early Galaxy Astrophysics Census Survey to study radial variations in the stellar population of 17 spectroscopically selected post-starburst (PSB) galaxies. We use spectral fitting to measure two Lick indices, H δ_A and Fe 4383 , and find that, on average, PSB galaxies have radially decreasing H δ_A and increasing Fe 4383 profiles. In contrast, a control sample of quiescent, non-PSB galaxies in the same mass range shows outwardly increasing H δ_A and decreasing Fe 4383 . The observed gradients are weak (≈ -0.2 Å/R_e), mainly due to seeing convolution. A two-SSP (simple stellar population) model suggests that intrinsic gradients are as strong as observed in local PSB galaxies (≈ -0.8 Å/R_e). We interpret these results in terms of inside-out growth (for the bulk of the quiescent population) versus star formation occurring last in the centre (for PSB galaxies). At $z \approx 0.8$, central starbursts are often the result of gas-rich mergers, as evidenced by the high fraction of PSB galaxies with disturbed morphologies and tidal features (40 per cent). Our results provide additional evidence for multiple paths to quiescence: a standard path, associated with inside-out disc formation and with gradually decreasing star formation activity, without fundamental structural transformation, and a fast path, associated with centrally concentrated starbursts, leaving an inverse age gradient and smaller half-light radius.

Key words: galaxies: evolution – galaxies: formation – galaxies: fundamental parameters – galaxies: high redshift – galaxies: starburst – galaxies: structure.

1 INTRODUCTION

At any given time, star-forming (SF) galaxies form a sequence in the mass–size plane (e.g. Shen et al. 2003; van der Wel et al. 2014); this mass–size relation is such that, at fixed stellar mass, SF galaxies are systematically larger than non-SF galaxies (hereafter, quiescent or Q galaxies). Moreover, the average size of both SF and Q galaxies increases with cosmic time (van der Wel et al. 2009; Fagioli et al. 2016; Williams et al. 2017). Given these properties, it is reasonable to assume that galaxies that have recently become quiescent have approximately the same size as SF galaxies of the same mass. This expectation is indeed consistent with the finding that, at fixed stellar mass, the youngest Q galaxies are also the largest (Wu et al. 2018).

There is, however, a class of objects, called post-starburst (PSB) galaxies, that have recently become quiescent, yet contrary to the above expectations are both: (i) smaller than coeval Q galaxies and (ii) much smaller than coeval SF galaxies (e.g. Whitaker et al. 2012; Almaini et al. 2017; Wu et al. 2018). Observationally, PSB galaxies (Dressler & Gunn 1983; Couch & Sharples 1987) present strong

★ E-mail: francesco.deugenio@gmail.com

Balmer-line absorption (typical of young, 0.3–1 Gyr-old stars) but lack H α emission (which excludes recent, $\lesssim$10 Myr star formation). Together, these two properties suggest that PSB galaxies stopped forming stars both *rapidly* (faster than $\approx$1 Gyr) and *recently* (within $\approx$1 Gyr of their look-back time). The empirical conjunction of compact structure with a rapid and recent transition to quiescence suggests that PSB galaxies followed a special evolutionary path, either an extreme version of normal galaxy evolution or some entirely different channel.

In the local Universe, PSB galaxies are empirically associated either with galaxy mergers (e.g. Zabludoff et al. 1996; Bekki, Shioya & Couch 2001; Yang et al. 2004; Goto 2005; Yang et al. 2008; Pracy et al. 2009; Wild et al. 2009; Pawlik et al. 2018) or with ram-pressure stripping in dense environments (Dressler et al. 1999; Poggianti et al. 1999; Tran et al. 2004; Poggianti et al. 2009; Paccagnella et al. 2019). They show a range of kinematic properties: from dispersion-dominated kinematics reminiscent of quiescent galaxies (and consistent with the outcome of mergers; Hiner & Canalizo 2015) to rotation-supported systems (e.g. Norton et al. 2001; Pracy et al. 2013; Owers et al. 2019). Chen et al. (2019) find that stellar kinematics depend on the location of the PSB regions within the target galaxy. In any case, even accounting for their relatively short visibility time, local PSB galaxies represent a marginal mode of galaxy evolution (Rowlands et al. 2018).

However, in the high-redshift Universe, PSB galaxies could be different. First, it appears that the fraction of PSB galaxies increases with cosmic time (e.g. Dressler et al. 1999; Poggianti et al. 1999; Wild et al. 2016, but see e.g. Balogh et al. 1997; Balogh et al. 1999; Muzzin et al. 2012, for a different view). Even if the fraction of PSB galaxies stayed constant, dense environments become rarer with increasing redshift (e.g. Carlberg et al. 1997; Younger, Bahcall & Bode 2005); hence, the physics underlying low- and high-redshift PSB galaxies could be different. This is not a surprising possibility, because the definition of PSB galaxies is purely empirical, and different quenching mechanisms could ostensibly leave similar or identical signatures. In addition, there is evidence for different structural properties between $z < 1$ and $z > 1$ PSB galaxies (Maltby et al. 2018), suggesting that redshift evolution might involve different physical processes.

A possible explanation of the observed properties of PSB galaxies is a central starburst in a previously normal galaxy. A significant amount of star formation inside $\approx$1 kpc from the centre of a galaxy can reduce its previous half-light radius, thus explaining the small observed size of PSB galaxies (Wu et al. 2020). At the same time, central starbursts are likely to undergo rapid quenching: either because of strong feedback or because of the short dynamical time in the central regions of galaxies, which leads to rapid consumption of the cold gas reservoir (e.g. Wang et al. 2019). However, without knowledge of the progenitors of PSB galaxies, it is impossible to establish whether they have always been compact or if their half-light radii have become smaller as a result of a central starburst and subsequent quenching.

Still, if the second hypothesis is true, we expect high-z PSB galaxies to exhibit clear evidence of a central starburst, such as outwardly increasing stellar age (as indeed observed in some local PSB galaxies; see e.g. Pracy et al. 2013; Chen et al. 2019; Owers et al. 2019). These inverse gradients are contrary to what is observed in the majority of both SF and Q galaxies: There is in fact overwhelming evidence that most galaxies form in an inside-out fashion. First, by comparing the size of the SF gas disc to the size of the stellar disc, the *instantaneous* radial growth rate of SF galaxies has been shown to be positive (Pezzulli et al. 2015; Nelson et al. 2016; Paulino-Afonso et al. 2017; Suzuki et al. 2019; Wang et al. 2019). Secondly, the stellar populations of most SF and Q galaxies have negative age gradients with radius (e.g. González Delgado et al. 2015; Zibetti et al. 2017): These gradients are qualitatively consistent with the outcome of inside-out growth *integrated* over cosmic time (Schönrich & McMillan 2017).[1] This is also true for individually measured stars in the Milky Way, both overall (i.e. the bulge is older than the disc, e.g. Valenti et al. 2013) and within the disc itself (Martig et al. 2016).

Measuring age gradients requires high-quality, spatially resolved spectroscopy in the optical rest frame, but until now these observations at intermediate/high redshifts have been out of reach or limited to small samples (Belli, Newman & Ellis 2017).

The Large Early Galaxy Astrophysics Census (LEGA-C; van der Wel et al. 2016) changed this state of affairs: LEGA-C provides the astrophysics community with deep spectra for $\gtrsim$3000 galaxies at a redshift of $z \approx 0.8$, when the Universe was only half its present age. In this work, we leverage the extraordinary depth of LEGA-C to study the structural imprint of inside-out or central-starburst growth in PSB galaxies at roughly half the age of the Universe. After introducing the data and the sample (Section 2), we show that PSB galaxies have distinctive gradients in their Lick indices, different from the control sample (Section 3) and consistent with an inverse age gradient (Section 4). We conclude this work with a discussion of the implications and with a summary of our findings (Section 5). Throughout this paper, we assume a flat lambda cold dark matter cosmology with $H_0 = 70$ km s^{-1} Mpc^{-1} and $\Omega_m = 0.3$ and a Chabrier initial mass function (IMF; Chabrier 2003). All magnitudes are in the AB system (Oke & Gunn 1983).

2 DATA ANALYSIS

2.1 The LEGA-C Survey

LEGA-C (van der Wel et al. 2016) is a deep spectroscopic survey targeting $0.6 < z < 1.0$ massive galaxies in the COSMOS field, using the VIMOS spectrograph (Le Fèvre et al. 2003) on the ESO Very Large Telescope. The LEGA-C primary sample consists of $\approx$3000 galaxies brighter than $K_s = 20.7 - 7.5\log[(1+z)/1.8]$, roughly equivalent to a mass-selection limit $\log M_\star/M_\odot > 10$. Each galaxy was observed for 20 h, reaching a typical signal-to-noise ratio of SNR ≈ 20 Å^{-1} in the continuum. The median seeing full width at half-maximum is FWHM = 1.0 arcsec, sampled with 0.205 arcsec spatial pixels, which is sufficient to extract spatial information (e.g. Bezanson et al. 2018; hereafter we refer to spatial pixels as spaxels and to spectral pixels simply as pixels). What sets LEGA-C apart from previous surveys is its unique combination of ultra-deep data, large sample size, and spatial resolution: These three characteristics enable us to study resolved stellar population properties in a statistically meaningful sample.

We use stellar masses $M_\star$ measured by fitting the 30 photometric bands of the UltraVISTA catalogue, covering the wavelength range 0.15–24 µm (Muzzin et al. 2013). Semimajor axis effective radii R_e were measured on *HST* ACS F814W images obtained as part of the COSMOS program (Scoville et al. 2007), using GALFIT (Peng et al. 2010) and the procedure of van der Wel et al. (2012). Spectroscopic redshifts were obtained by fitting the galaxy spectra with a library of

[1] Contrary to this picture, there is considerable evidence that some Q galaxies have positive or U-shaped age gradients (La Barbera et al. 2012; Zibetti et al. 2020). As it will become clear, this fact by itself does not contradict the picture we present in this paper.

synthetic stellar population models (Conroy et al., in preparation), following the procedure highlighted in Bezanson et al. (2018). Rest-frame $U - V$ and $V - J$ colours were calculated by fitting a set of seven template spectra to the UltraVISTA SED photometry (see Straatman et al. 2018, for a full description).

2.2 Sample selection

Our parent sample is taken from the LEGA-C public Data Release 2 (Straatman et al. 2018), selected to have $f_{\rm use} = 1$ (1462 galaxies; see Straatman et al. 2018, for the definition of the quality flag $f_{\rm use}$), with four or more radial bins with SNR $> 10\,{\rm pixel}^{-1}$ each (see Section 2.3; 614 galaxies), and with $R_{\rm e} > 0.5 \times$ (FWHM/2.355), where the seeing FWHM was measured directly on the slit images of each galaxy, using *HST* photometry as unconvolved reference (van Houdt in preparation; 603 galaxies). We identify passive galaxies in this sample using the $U - V$ versus $V - J$ colour–colour diagram (cf. Labbé et al. 2005; van der Wel et al. 2016; 298 galaxies), and we select 17 PSB galaxies[2] as having a median index over the spatial measurements H$\,\delta_{\rm A} \geq 4$ Å, corresponding to an approximate simple stellar population age of 1–1.5 Gyr, and typically adopted as selection threshold for spectroscopically selected PSB galaxies (Wu et al. 2018).[3] The combination of colour and absorption-strength selection criteria is robust against contamination from dust-obscured starbursts (see e.g. Wu et al. 2018, and Dressler et al. 1999; Poggianti et al. 1999). Other authors have used a cut on inclination (Pawlik et al. 2018), but we find that inclination does not drive our results; hence, no inclination cut has been applied (see Section 3.1). These PSB galaxies consist of six centrals, six isolated, three satellites, and two where no environment could be assigned (Darvish et al. 2017). As such, we can exclude that this sample is dominated by satellites or subject to ram-pressure stripping. As a control sample, we take 141 passive galaxies having the same mass *range* as the PSB sample, but median H$\,\delta_{\rm A} < 4$ Å. Choosing a stricter cut in H$\,\delta_{\rm A}$ does not change the properties of the control sample, because the bulk of the control galaxies have H$\,\delta_{\rm A}$ well below 4 Å (only 14 galaxies have median H$\,\delta_{\rm A}$ between 2.5 and 4.0 Å). Even though a control sample having the same mass *distribution* as the PSB sample would be better suited to control for mass-related biases, in practice such selection is not possible with our data (see Section 3.1 for a discussion).

The position of the PSB galaxies on the mass–size plane is illustrated in Fig. 1, where each target is represented by its *HST* image, so that each inset is placed at the approximate location of the galaxy portrayed (each inset was allowed a maximum offset of 0.2 dex in $\log M_\star$ and 0.1 dex in $\log R_{\rm e}$, to avoid overlappings).

We use *HST* imaging to assign to each galaxy a probability that it underwent a recent merger. Three astronomers visually inspected the galaxies and the residuals of the best-fitting GALFIT models, looking for two merger signatures: tidal features and double cores. Notice that close neighbours are not classified as mergers, unless tidal features are visible either in the *HST* image or in the residuals. Galaxies were classified as either mergers (score of 1) or non-merger (score of 0). The average score is the probability that a given target is a merger

[2]The total was 19 galaxies, but we further discarded two targets contaminated by interlopers.

[3]The selection is almost unchanged (one galaxy is changed) if we use the value of the integrated H$\,\delta_{\rm A}$, as expected from the excellent agreement between the median and integrated index measurements (see Fig. 3). Moreover, we note that our results are qualitatively unchanged if we use a stricter selection threshold at H$\,\delta_{\rm A} \geq 5$ Å.

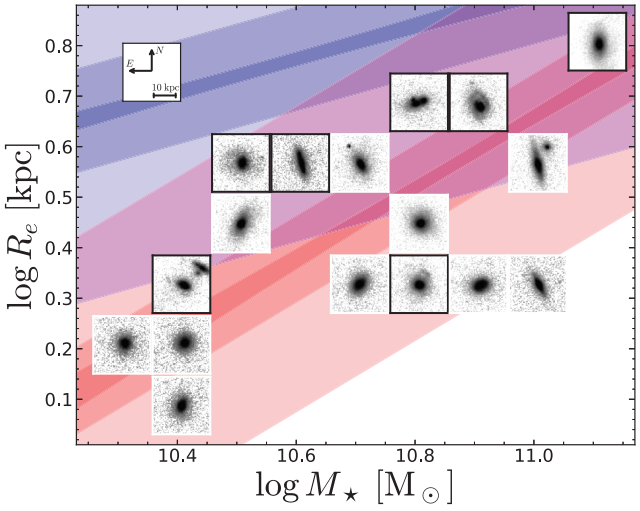

Figure 1. Our sample of PSB galaxies has a range of masses, sizes and morphologies, including 40 per cent of mergers. Galaxies with P(merger) ≥ 0.5 are highlighted using solid black contour insets. Each image is a 10×10 arcsec^2 cut-out from *HST* ACS F814W, and the inset centre is placed at the approximate location on the mass–size plane of the portrayed galaxy (offsets of up to 0.2 dex are allowed for display purposes). The orientation and median physical scale of the images are indicated in the top left inset. The red (blue) transparent regions indicate the best-fitting linear model to the mass–size relation for quiescent (SF) galaxies; from darkest to lightest, the regions highlight the 95 per cent confidence interval, the 68 per cent prediction interval, and the 95 per cent prediction interval. The best-fitting parameters for the mass–size relations were derived using the least-trimmed squares algorithm (Rousseeuw & Driessen 2006; Cappellari et al. 2013). Despite our spatial resolution constraint, which systematically selects the largest PSB galaxies, the sample lies appreciably below the SF mass–size relation for LEGA-C.

remnant. Galaxies with a score P(merger) ≥ 0.5 are highlighted by insets with solid black contours in Fig. 1. For PSB galaxies, we find 7/17 or 40 per cent of mergers.

Galaxies with/without detectable merger signatures have consistent values of the integrated H$\,\delta_{\rm A}$ (mean $\langle {\rm H}\,\delta_{\rm A}\rangle = 5.91 \pm 0.45$ and 5.49 ± 0.28 Å, respectively) and Fe 4383 (mean $\langle {\rm Fe}\,4383\rangle = 1.75 \pm 0.36$ and 2.34 ± 0.37 Å, respectively). However, we find that galaxies with integrated H$\,\delta_{\rm A}$ larger than the median value (H$\,\delta_{\rm A} \geq 5.54$ Å) have somewhat smaller size than galaxies with H$\,\delta_{\rm A} < 5.54$ Å), but the significance is only two standard deviations. Still, the direction of this anticorrelation between H$\,\delta_{\rm A}$ and half-light radius is the same reported in Wu et al. (2020) for a larger PSB sample. Nevertheless, we find that splitting the sample at P(merger) ≥ 0.5 or at the median value of the half-light radius does not change our results, apart from lowering their statistical significance (Section 3.1).

2.3 Spatially resolved Lick index measurements

We measure Lick indices, defined as in Worthey & Ottaviani (1997) and Trager et al. (1998), as well as the D_n4000 index (Balogh et al. 1999). The method we use, developed by Scott et al. (2017) and Barone et al. (2020), can be thought of as a non-parametric emission-line subtraction. The goal of their algorithm is to leverage spectral information away from emission-line regions to reconstruct the galaxy stellar spectrum inside such regions. Empirical stellar spectra have been shown to encode significantly more information per spectral element compared to synthetic spectra (e.g. Martins & Coelho 2007; Plez 2011); therefore, they are more likely to accurately

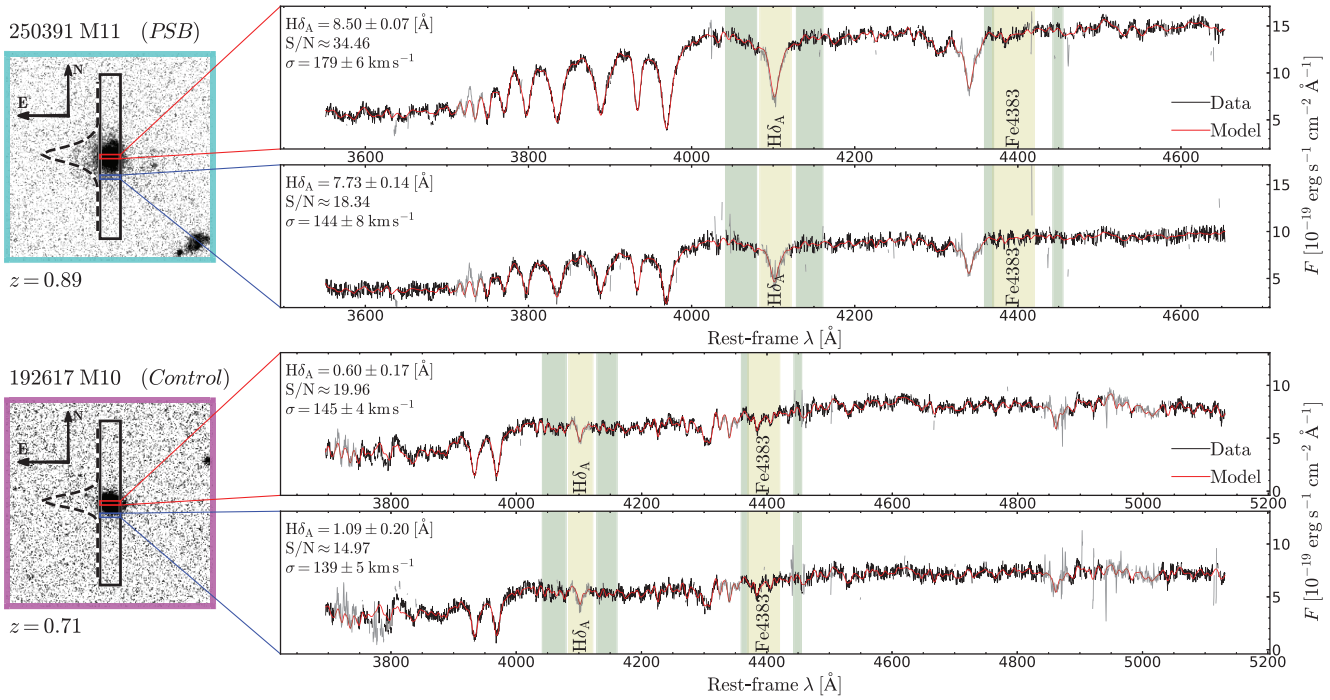

Figure 2. Central and outer rest-frame spectra for the PSB galaxy M11.250391 (top) and for the quiescent galaxy M10.192617 (bottom). The continuum and the index regions for the Lick indices H δ_A and Fe 4383 are highlighted in green and yellow, respectively. The approximate spaxel position for each spectrum is marked on the finding chart. For the quiescent galaxy, H δ_A is higher in the outskirts than that in the centre, and for the PSB galaxy H δ_A is strongest in the centre. The black lines represent the LEGA-C data, whereas the red lines are the pPXF best-fitting models (see Section 2.3 for more details). Regions of the spectrum where the data were masked are rendered in grey: These regions are excluded either because they fail a 3σ clipping threshold or because of possible emission lines (regardless of whether line emission has been detected).

reproduce the observed galaxy spectra (e.g. van de Sande et al. 2017, their fig. 25), and to capture the necessary information to reconstruct the spectrum in the masked regions. For this reason, we fit the LEGA-C spectra with an empirical stellar template library. We use the MILES stellar template library because of its generous range in stellar classes (Sánchez-Blázquez et al. 2006; Falcón-Barroso et al. 2011), but we obtain equivalent results using the high-spectral resolution ELODIE library (Prugniel & Soubiran 2001).

We fit the stellar continuum using the penalized Pixel Fitting code pPXF (Cappellari & Emsellem 2004), following the procedure developed by Scott et al. (2017). In short, we fit the spectrum optimizing for the template weights, for the first and second moments of the line-of-sight velocity distribution, v and σ, and for a 12th-order additive polynomial.[4]

The fit is performed in three iterative steps. The first iteration is used to estimate the noise spectrum; the second iteration is used to identify weak emission lines and bad pixels and the third and final gives the best-fitting parameters. The spectrum in bad pixels and in regions of line emission is replaced by the best-fitting stellar spectrum. This step is especially important for the Balmer absorption indices, which overlap regions of nebular emission. Whether the higher order Balmer lines are masked or not does not affect our results (Hϵ and bluer; Barone et al. 2020).

Once the emission-line-corrected spectra are determined, each index is measured after convolving the spectrum with a Gaussian, so that the final spectral resolution matches the spectral resolution of the relevant index. For more details on the fitting and measurement procedure, refer to Scott et al. (2017).

In order to guarantee an acceptable precision, we bin the slit spectra out from the central spaxel to guarantee an SNR $= 10\,\mathrm{pixel}^{-1}$. First, we fit the individual spectra, to estimate their SNR. We then fold the slit about the central spaxel, ranking the spectra by their distance to the centre. Starting from the central spaxel, we create spatial bins by summing adjacent spaxels until the target SNR is met. For galaxies with obvious contamination, we consider only the half of the spectrum away from the companion or interloper object. Two example fits are shown in Fig. 2.

For our analysis, we focus on two indices: H δ_A and Fe 4383. There are two reasons for this choice: First, it represents a minimal index set that is able to break the age–metallicity degeneracy, at least for the age range relevant to PSB galaxies. In particular, H δ_A has a local maximum for an $\approx$0.3 Gyr-old simple stellar population (Worthey & Ottaviani 1997; Kauffmann et al. 2003), so that it is not possible to invert the age-H δ_A function using H δ_A alone. However, for the ages and metallicities relevant to this work, adding Fe 4383 allows us to break this age degeneracy (see Section 4.1). Secondly, these indices ensure uniform coverage across the largest possible sample, whereas indices defined at redder wavelengths drop out of the LEGA-C observed range with increasing redshift.

Each index measurement has a measurement uncertainty, derived from the residuals of the spaxel spectrum with respect to the best-

[4]Even though this choice is motivated by convergence criteria (i.e. higher degree polynomials do not exhibit faster variation with wavelength), we find that the value of the Lick indices does not change for degrees higher than 2. This behaviour is due to a combination of the local nature of the Lick measurements and of our good data quality. Replacing additive polynomials with multiplicative polynomials does not change our results either (see also Bezanson et al. 2018).

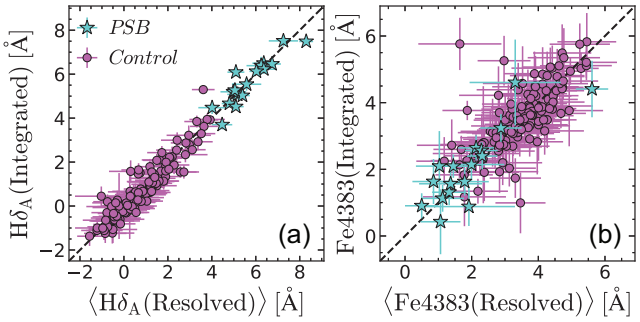

Figure 3. We find very good agreement between the median of the spatial measurements and the measurement on the integrated slit profile, for both H δ_A and Fe 4383 (panels a and b, respectively). The cyan stars are PSB galaxies, and the magenta circles are the control sample of quiescent galaxies (the errorbars have been rescaled). The best-fitting relations have slopes of 0.96 ± 0.03 (for H δ_A) and 1.03 ± 0.08 (for Fe 4383), consistent with unity. The observed scatter about the best-fitting relations is $\Delta = 0.26$ and $\Delta = 0.52$, respectively, consistent with the measurement uncertainties (after rejecting 3σ outliers, the reduced χ^2 value is 1.01 in both cases).

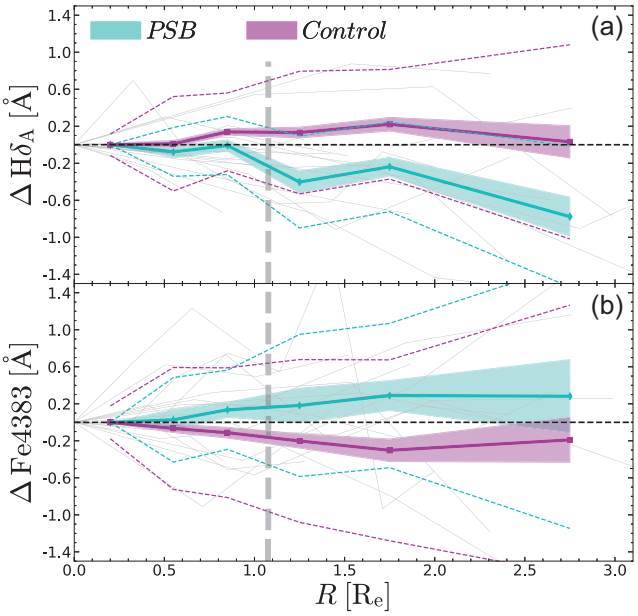

Figure 4. Unlike control galaxies (magenta), PSB galaxies (cyan) show decreasing H δ_A and flat Fe 4383 , clear signatures of a central starburst. The solid lines trace the running median of our measurements and the uncertainties about the median are enclosed by the shaded regions, whereas the coloured dashed lines enclose the 16 and 84th percentiles of the data. The vertical dashed lines marks the σ-equivalent of the median seeing. Thin grey lines trace the profile of individual PSB galaxies, showing that besides the average trend, individual galaxies present a range of radial profiles (individual control galaxies are not shown). The observed PSB trends are highly significant: In the most conservative estimate, the probability of a false positive is $P = 10^{-4}$.

fitting spectrum. We find that these values are underestimated and we derive an upscaling factor as follows. Given the relatively high SNR in the central spaxels, we often have two measurements at a given distance from the centre, one for each side of the slit. We assume that galaxies are symmetric about their centre, so we can use the difference between the two measurements to rescale the formal uncertainties on our measurements. Comparing the measurements from either side of the galaxies, we find no systematic offset, but the standard deviation is larger than the formal uncertainties. We rescale the formal uncertainties by a factor that depends on the Lick index being considered and on the value of the SNR. Given that the SNR depends strongly on the distance from the centre of each galaxy, our SNR rescaling factors are effectively a function of radius. For H δ_A , the factor ranges from 1 (at the highest SNR) to 3 (for $10 < \mathrm{SNR} < 15\,\mathrm{pixel}^{-1}$). For Fe 4383 , the factor ranges from 1 to 2.5. Similar results were obtained following the method of Straatman et al. (2018), i.e. using repeat observations of 61 galaxies to assess the random uncertainties on the Lick index measurements. The main difference with our method is that using repeat observations tends to overestimate the uncertainty for PSB galaxies, which have systematically stronger H δ_A absorption compared to the sample of repeat observations (only one PSB galaxy has two observations).

In Fig. 3, we compare the value of the integrated Lick indices from Straatman et al. (2018) to the (unweighted) median value for our resolved measurements. We show separately the PSB and control sample as cyan stars and magenta circles, but we fit a single relation to both sets, and find excellent agreement between the two measurements. For H δ_A, we find a best-fitting linear slope of 0.96 ± 0.03 and a root mean square residual along the y-axis of 0.33 Å (panel a). Thus, the best-fitting relation is statistically consistent with the identity. As for the scatter, if we assume that the precision of the two determinations is the same and that there was no intrinsic scatter (due e.g. to systematic errors), we can estimate the average measurement uncertainty as $0.26/\sqrt{2} = 0.18$ Å. *Mutatis mutandis,* similar considerations apply to Fe 4383 ; here the best-fitting linear relation has a slope of 1.03 ± 0.08 and an observed scatter of 0.51 (panel b). In principle, a comparison between the unweighted median and the integrated indices is biased, because the latter are *de facto* flux weighted. However, if we repeat the above comparison after replacing the unweighted median indices with the inverse-error weighted indices, the results are statistically consistent with what we have reported for the unweighted median (except for the best-fitting slope of the H δ_A relation, which goes from 0.96 ± 0.03 to 1.09 ± 0.02). This consistency is probably due to the mix of PSB and non-PSB galaxies, because, as we will argue in the next section, these two sets have different radial properties. These properties are likely to impart opposite biases on the unweighted median indices compared to the integrated indices. Galaxy 107643 M4 is the most prominent outlier in Fig. 3 (more than three standard deviations), but it has a relatively bright interloper that might affect the integrated spectrum. This galaxy is part of the control sample, and its inclusion or removal does not change the outcome of our analysis.

When we repeat our analysis with the ELODIE stellar template library, we find excellent agreement in the average value of the indices: Considering only spectra with $\mathrm{SNR} \geq 10\,\mathrm{pixel}^{-1}$, we find no mean offset in either H δ_A and Fe 4383 (ΔH $\delta_A = -0.001 \pm 0.002$ Å and ΔFe 4383 $= 0.012 \pm 0.009$ Å).

3 RESULTS

In Fig. 4(a), we show the average radial trends of H δ_A relative to the central value, for both PSB galaxies (cyan) and the control sample (magenta). The radial profiles of individual galaxies have been binned in R_e, with the lines tracing the (moving) inverse-variance-weighted median. The uncertainty on the median is encompassed by the shaded region (estimated as the semidifference between the inverse-variance-weighted 16 and 84th percentiles, divided by the square root of the number of measurements in each bin). The dashed lines enclose the 16 and 84th percentiles of the distribution. The

control sample of quiescent, non-PSB galaxies and the PSB sample have opposite radial trends: The control sample has a weak positive $H\delta_A$ gradient. In contrast, PSB galaxies have on average decreasing $H\delta_A$ profiles, i.e. the $H\delta_A$ index is highest in the central regions and lowest in the outskirts. For the Fe 4383 index (Fig. 4b), we find that PSB galaxies have a radially increasing profile, whereas the control sample has decreasing Fe 4383 with radius. Similar results are obtained for other empirical spectral indices, which we do not show for brevity: for example, PSB galaxies have decreasing $H\gamma_A$ and flat D_n4000, whereas control galaxies have increasing $H\gamma_A$ and decreasing D_n4000 (see Appendix A).

If we assume that PSB galaxies have flat $H\delta_A$ gradients, we can calculate the probability of measuring by chance a negative gradient as follows: For each radial measurement, we take the distance between the median $H\delta_A$ and zero (the value expected from a flat gradient; this is equal to $\Delta H\delta_A$). We then divide this distance by the uncertainty on $\Delta H\delta_A$, and calculate the resulting one-tailed probability of a value exceeding the measurement (we assume a Gaussian distribution). The number of independent radial measurements in the stacked profiles is difficult to calculate, because each galaxy has different size and slightly different seeing. We therefore provide the results for the most conservative case only, i.e. assuming only two independent radial measurements. Assuming that PSB galaxies have flat $H\delta_A$ radial profiles, the probability of finding by chance a negative gradient is $P = 10^{-4}$. For the Fe 4383 gradients, using the same assumptions we get $P = 0.04$. Bootstrapping 75 per cent of our data yields $P = 0.06$ and 0.04 respectively. Similarly, the probabilities that the control sample has flat profiles for $H\delta_A$ and Fe 4383 are $P = 0.02$ and 0.07, respectively (bootstrapping yields $P = 10^{-3}$ and 10^{-4}). Combining these opposite trends naturally leads to even smaller probabilities that PSB and control galaxies have the same profiles: $P = 10^{-5}$ and 0.01, respectively, for $H\delta_A$ and Fe 4383 (bootstrapping yields $P =$ 0.03 and 0.01). We assume that three independent radial bins yield P-values that are 5–10 times smaller.

3.1 Caveats

The results are qualitatively unchanged if we measure the distance along the slit in physical units; however, since physical units may compound radial trends *within* galaxies with size trends *between* galaxies, they are not considered here.

We remark that the extent of our measurements is comparable to the FWHM of the atmospheric seeing (the vertical dashed line in Fig. 4 is the seeing equivalent σ, defined as FWHM/2.355; see Section 2.2). The value shown is the median seeing for the 17 PSB galaxies, expressed in units of the galaxy R_e, and falls approximately at one R_e. For this reason, the gradients measured here are much flatter than the intrinsic gradients (Section 4), in agreement with what is observed for PSB galaxies at $z \approx 0.1$ (Pracy et al. 2013). The fact that the seeing is comparable to the median effective R_e of our PSB sample might explain the change in slope around $R \approx 2\,R_e$, but we cannot exclude the presence of a size-dependent bias for this bin (only 13/17 measurements for the PSB sample, only 36/141 measurements for the control sample).

Due to the small sample size, we are unable to study the relation between inverse gradients and other galaxy properties. However, we find that the trend is qualitatively unchanged if we consider mergers and non-mergers separately, indicating that our results are not driven by prominent morphologic asymmetries. The same is true if we split the PSB sample in two at the median value of the Sérsic index ($0.6 \leq n \leq 6$; the median is 2.9), or at the median value of the apparent effective radius ($0.2 \leq R_e \leq 0.7$; the median is 0.3 arcsec), or at the median value of stellar mass ($10^{10.3} \leq M_\star \leq 10^{11.2}$; the median value is $10^{10.68}\,M_\odot$), or at the median value of the axial ratio ($0.21 \leq q \leq 0.94$; the median value is 0.64). Finally, we repeat the analysis limiting the selection to PSB classified as central or isolated only: The trends are again qualitatively unchanged, ruling out that our results are due to environment effects on satellite galaxies.

In Section 2.2, in order to ensure that the study is not limited by the size of the control sample, we selected control galaxies to have the same mass range as the PSB sample. Admittedly, a better choice would be to select control galaxies having the same mass *distribution* as the PSB sample, because the strength of stellar population gradients of passive galaxies depends on stellar mass and velocity dispersion (e.g. Martín-Navarro et al. 2018; Zibetti et al. 2020). However, the quiescent, non-PSB galaxies that make up the control sample have on average lower SNR and larger measurement uncertainties than PSB galaxies of the same mass. For this reason, imposing the same mass distribution between the PSB and control samples results in too few control galaxies (25) with too large measurement uncertainties to constrain the sample properties. Nevertheless, we find that the mass-matched control sample is statistically consistent with the actual control sample used in this work. To further test the effect of mass-dependent bias in the observed gradients, we split the control sample in two subsets at the value of its median stellar mass $10^{10.82}\,M_\odot$. We find that both subsets have gradients that are statistically consistent with the control sample, but the most massive half of the sample has steeper Fe 4383 gradient than the least massive half, in qualitative agreement with observations of local galaxies [e.g. Martín-Navarro et al. (2018) find that the most massive elliptical galaxies have steeper radial metallicity gradients]. Using either half of the control sample would not change the nature of our results.

Incidentally, the fact that PSB galaxies have opposite radial trends compared to the general population suggests that our results are unlikely to arise from bias due to decreasing SNR with radius.

4 A TWO-SSP TOY MODEL

To interpret the observed trends, we implement a six-parameter model to predict the stacked measurements of Fig. 4. As a light profile, we use a one-dimensional Sérsic model, where the spectrum at each radius is the superposition of two simple stellar populations (SSPs; i.e. each population has uniform age and metallicity). As SSP spectra we take the MILES models (Vazdekis et al. 2010, 2015), using BaSTI isochrones (Pietrinferni et al. 2004, 2006), solar [α/Fe], and Chabrier IMF (Chabrier 2003). The resulting grid of 636 spectra spans $-2.27 < [Z/H] < 0.40$ and $0.03 < \text{age} < 14.00$ Gyr [replacing BaSTI with Padova isochrones from Bertelli et al. (2009) yields qualitatively consistent results]. Our model superimposes two SSPs, representing the central stars and the stars in the outskirts of the galaxy, labelled, respectively, as 'in' and 'out' (the corresponding SSP parameters are age_{in}, $[Z/H]_{\text{in}}$, age_{out}, and $[Z/H]_{\text{out}}$). The mass fraction of the 'in' SSP to the total is given, at each radius R, by

$$f(R) = f_0 \frac{\exp\left(\frac{R_m - R}{R_d}\right) - 1}{\exp\left(\frac{R_m}{R_d}\right) - 1} \tag{1}$$

where R is expressed in units of R_e, and $R_m = 6\,R_e$ is an arbitrary radius that is 'large' relative to the extent of our measurements. f is a declining exponential function, scaled so that the central value is $f(0) = f_0$ and downshifted so that $f(R_m) = 0$. This choice is motivated as follows. First, stellar generations tend to form superimposed

exponential discs (Buck et al. 2019; Poci et al. 2019 – and the ratio of two exponentials is also exponential). Secondly, there is evidence that PSB galaxies host rotation-supported discs (Hunt et al. 2018). The parameter R_d specifies the concentration of the central SSP: For any non-negative value, R_d is the exponential scale radius of $f(R)$, in the sense that $\partial_R f = -f/R_d + \text{const.}$ (smaller values of R_d correspond to more concentrated central populations). As $R_d \to \infty$, we have $f(R) \to (1 - R/R_m)$: In other words, using equation (1) to express $f(R)$ includes both a physically motivated exponentially declining fraction and a linear mixing fraction that represents the simplest uninformed guess. In practice, we implement the infinite range in R_d by parametrizing this scale radius as $\tan\vartheta_d$, with $0 \leq \vartheta_d \leq \pi/2$. Thus, the fraction f requires two additional parameters: f_0 and ϑ_d. For our purposes, f_0 and ϑ_d are just nuisance parameters: Given (i) our spatial resolution and (ii) the use of a stack analysis, we cannot meaningfully constrain the *structure* of PSB galaxies, but just the sign of radial gradients of stellar age and metallicity. The Sérsic profile has arbitrary central surface brightness and R_e, but the Sérsic index is fixed at $n = 2.4$, the median value for the PSB sample. The model is convolved with a Gaussian point spread function (PSF) with $\sigma = 1\,R_e$ (see Fig. 4). In summary, our most general model has six free parameters, the age and metallicity for each of the two SSPs, and two more parameters to specify the (monotonic) radial mixing of these two SSPs. The likelihood of the data given these model parameters is expressed as a multivariate Gaussian over the observed H$\,\delta_A$ and Fe 4383 measurements. We assume flat priors on all the model parameters, with the allowed range equal to the physical range of each parameter: $0.03 < \text{age}_{in}, \text{age}_{out} < 14.00$ Gyr, $-2.27 \leq [Z/H]_{in}, [Z/H]_{out} \leq 0.40$, $0 \leq \vartheta_d \leq \pi/2$, and $0 \leq f_0 \leq 1$. We combine the likelihood and priors to write the posterior distribution (apart from the evidence), and we estimate the model parameters by integrating the posterior distribution with the Markov chain Monte Carlo approach (Metropolis et al. 1953).

Constraining this six-parameter model using twelve measurements is problematic, but our goal is not to infer an accurate value of the parameters. We use the model as a benchmark, to assess the plausibility of less general sub-models, obtained by constraining some of the six parameters from the general model, and we show that any acceptable solution has properties that are inconsistent with the properties of the control sample.

4.1 The benchmark model for PSB galaxies

The results for the most general PSB model are shown in Fig. 5. Panel (a) shows the posterior distribution for the six model parameters, marginalized over all possible sets of four and five parameters. A summary of the model results is reported in Table 1. For ease of comparison, the posterior distributions of age_{in} and age_{out} and of $[Z/H]_{in}$ and $[Z/H]_{out}$ are also reported in panel (b) (using a logarithmic scale for age). Panel (c) compares the measured Lick indices (cyan stars with errorbars) to the prediction of the most likely model (i.e. the mode of the posterior distribution); the dashed and solid grey lines trace, respectively, the intrinsic profile and the seeing convolved profile. Within one R_e, the intrinsic H$\,\delta_A$ gradient for our stacked profile is $\approx -0.76 \pm 0.03$ Å$/R_e$, consistent with the median value for local PSB galaxies (-0.83 ± 0.23 Å$/R_e$; Chen et al. 2019. We considered both their 'central' and 'ring-like' PSBs to calculate the median, consistent with our sample selection criteria that do not differentiate between different PSB morphologies. The fit was performed using weighted least-squares optimization.)

The corner plot shows the well-known age–metallicity degeneracy (Worthey 1994), for each of the two SSPs independently. The Spearman rank correlation coefficient is $\rho = -0.39$ for age_{in} and $[Z/H]_{in}$ and is $\rho = -0.52$ for age_{out} and $[Z/H]_{out}$ (panel a; all P-values are zero owing to the large number of sample points). Of all the possible parameter pairs, we find the strongest degeneracy between f_0 and age_{in} ($\rho = 0.84$); this can be interpreted as the degeneracy between the burst fraction (governed by the central value f_0) and the burst age (Serra & Trager 2007).

With these degeneracies in mind, we can inspect panel (b), which reports the age and metallicity histograms of the two SSPs on the same scale: Here the central SSP (solid blue histogram) has both younger age and lower metallicity than the outer SSP (red dashed histogram). For SSP age, we find $\text{age}_{in} = 0.48^{+0.23}_{-0.21}$ Gyr and $\text{age}_{out} = 1.28^{+0.43}_{-0.20}$ Gyr (here and in the following, the results quoted refer to the 50th and the uncertainties encompass the 16 and 84th percentiles of the relevant posterior distribution). For metallicity, the results are $[Z/H]_{in} = -0.13^{+0.33}_{-0.22}$ and $[Z/H]_{out} = 0.10^{+0.17}_{-0.06}$. We find that metallicity is not well constrained, as expected from young SSPs. However, while the difference in [Z/H] is not statistically significant (within one standard deviation), the age difference is larger than 3.5 standard deviations: The probability P that the two SSPs have the same age is $P < 2 \times 10^{-4}$ (this value assumes a Gaussian distribution and is the most conservative result; using the marginalized posterior distribution, we obtain $P < 1.3 \times 10^{-6}$). The strong separation between the age of the two SSPs is mostly due to the sharp cut-off in the posterior distribution of age_{out} below $\approx$0.9 Gyr (red dashed age histogram in panel b). This strong cut-off may be surprising, because H$\,\delta_A$ has a local maximum at 0.1–1 Gyr (the exact value depends on metallicity; see e.g. Worthey & Ottaviani 1997 and Kauffmann et al. 2003, their fig. 2), so that there is a strong degeneracy between H$\,\delta_A$ and SSP age precisely where the model infers a cut-off in the distribution. The solution to this apparent conundrum is in the value of Fe 4383 : At fixed metallicity, Fe 4383 increases with SSP age. For this reason, even though age_{out} younger than 0.9 Gyr could indeed explain the decreasing values of H$\,\delta_A$ with radius, it would also predict a radially decreasing Fe 4383 , opposite to what is observed. In addition, even for the highest metallicity, SSPs young enough to have H$\,\delta_A \lesssim 4$ Å have Fe 4383 < 0 Å, inconsistent with the observations. Notice also that while $\text{age}_{in} < \text{age}_{out}$, we do not find an 'old' outer SSP: this is due to the use of a single SSP instead of an extended star formation history (SFH), as we show in Section 4.4. We conclude that this model, simple yet general, strongly prefers an age gradient over a metallicity gradient to explain the median index profiles observed in our PSB sample.

4.2 Modelling the control sample

We have already ruled out the possibility that the median gradient of the PSB and of the control sample are the same. However, could these different gradients arise from similar stellar populations, observed at different ages? This question is paramount to understanding whether (in an average sense) the control sample is consistent with passive evolution of the PSB sample. To give an answer, we apply our toy model to the median Lick profiles of the control sample. The results are illustrated in Fig. 6, where the meanings of the symbols are the same as in Fig. 5. The model predictions are compared to the data in panel (c): Within one R_e, we find an H$\,\delta_A$ gradient of $\approx$1 Å$/R_e$, whereas outside one R_e the intrinsic index profile is flat. This behaviour results from the combination of a relatively high central fraction (see the posterior probability of f_0 in panel a) and compact spatial distribution (small ϑ_d). This behaviour, however, may not be robust, given the strong degeneracy between f_0 and ϑ_d, which affects the intrinsic radial gradients ($\rho = -0.76$). We also remark

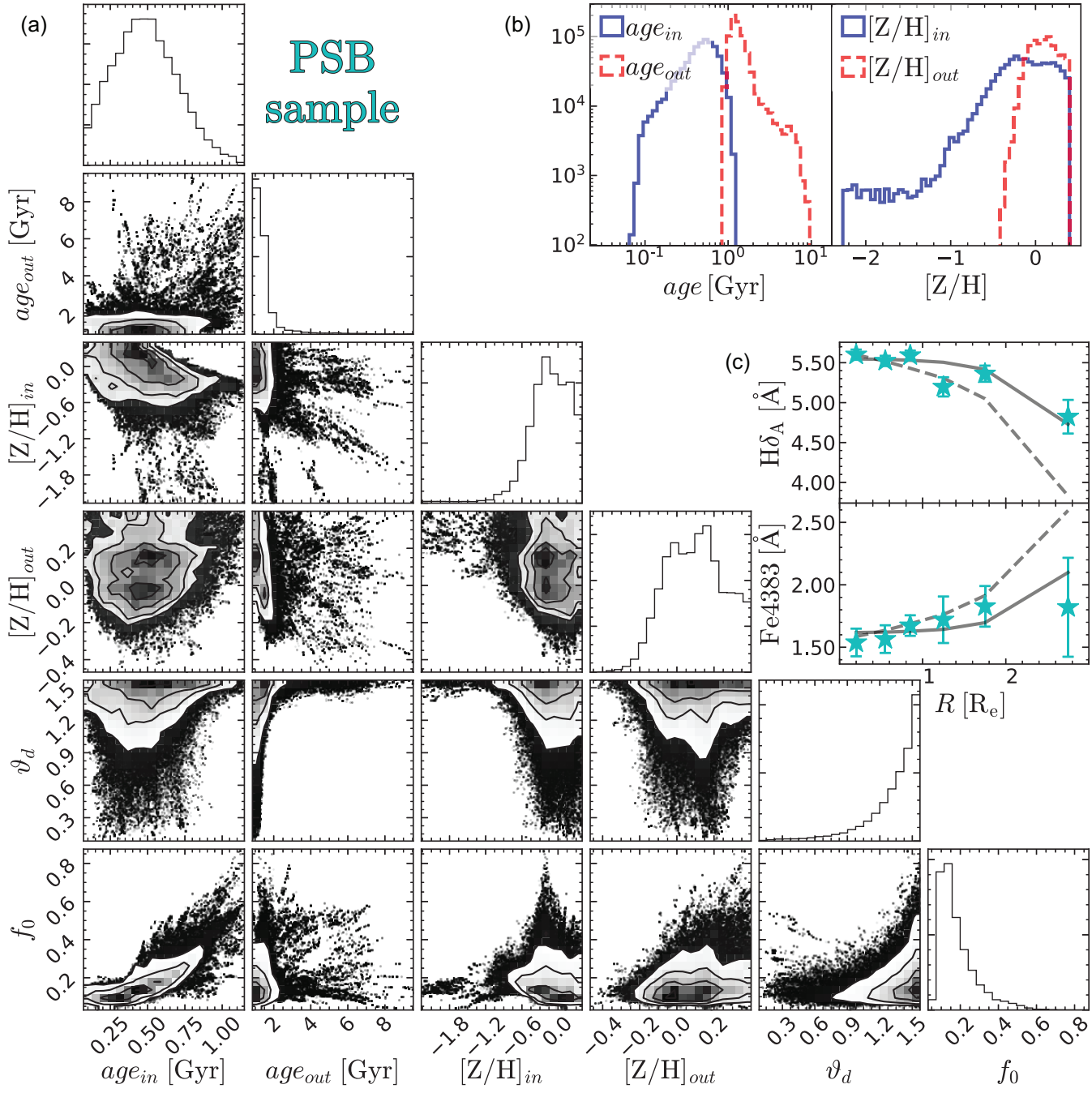

Figure 5. Our two-SSP toy model requires inverse age gradients in PSB galaxies (Panel a). The model uses two SSPs with different spatial distributions to reproduce the median observed gradients in both H δ_A and Fe 4383 (Panel c). The dashed/solid lines show the model prediction before/after seeing convolution, and the cyan stars trace the median index values for the PSB sample. The ages of the inner and outer SSPs are clearly different: The inner SSP (solid blue histogram in panel b) is clearly younger than the outer SSP (dashed red histogram). In contrast, SSP metallicities are consistent within the uncertainties. The corner diagram shows the marginalized probability for the model; the strongest correlation is between f_0 (tracing the burst fraction) and age_{in} (tracing the burst age).

that the last radial measurement appears to be an outlier: ignoring this point yields a less steep gradient of ≈ 0.8 Å$/R_e$.

Examining the corner diagram (panel a), we find again that age and metallicity anticorrelate for each SSP ($\rho = -0.10$ and -0.31 for the inner and outer SSPs, respectively). However, compared to the posterior probability distribution for the PSB sample, for the control sample these degeneracies are significantly smaller (in absolute value). On the other hand, we find a strong correlation of the metallicity of the inner SSP ($[Z/H]_{in}$) with both age and metallicity of the outer SSP: We find $\rho = 0.61$ for age_{out} and $\rho = -0.72$ for $[Z/H]_{out}$. These strong correlations are likely due to metallicity being the strongest driver of both H δ_A and Fe 4383 for old stellar populations; their presence highlights the need for comprehensive modelling in order to interpret our data.

Table 1. Summary of the two-SSP models. PSB galaxies are best described by an inverse stellar population structure, i.e. centre younger and/or lower metallicity than the outskirts. Imposing an inside-out age structure on PSB galaxies yields a poor fit (reduced $\chi^2 \approx 6$). On the contrary, control galaxies are best described by an inside-out stellar population structure.

Model name	Constraints	age_{in} Gyr	age_{out} Gyr	$[Z/H]_{in}$	$[Z/H]_{out}$	ϑ_d	f_0	χ^2_ν	Structure
(1)	(2)	(3)	(4)	(5)	(6)	(7)	(8)	(9)	(10)
PSB (benchmark)	none	$0.48^{+0.23}_{-0.21}$	$1.28^{+0.43}_{-0.20}$	$-0.13^{+0.33}_{-0.22}$	$0.10^{+0.17}_{-0.06}$	$1.41^{+0.13}_{-0.29}$	$0.15^{+0.11}_{-0.05}$	1.9	inverse
Control (benchmark)	none	$8.3^{+3.9}_{-4.2}$	$2.27^{+0.05}_{-0.08}$	$0.21^{+0.13}_{-0.19}$	$-0.15^{+0.04}_{-0.04}$	$0.26^{+0.28}_{-0.13}$	$0.75^{+0.15}_{-0.14}$	3.5	inside-out
PSB inside-out age	$age_{in} \geq age_{out}$	$3.95^{+7.70}_{-3.10}$	$0.85^{+0.02}_{-6.28}$	$0.08^{+0.18}_{-0.69}$	$0.15^{+0.07}_{-0.10}$	$1.20^{+0.34}_{-0.87}$	$0.40^{+0.59}_{-0.34}$	6.0	inside-out (age) inverse (metallicity)
PSB inside-out metallicity	$[Z/H]_{in} \geq [Z/H]_{out}$	$0.68^{+0.12}_{-0.11}$	$9.84^{+2.99}_{-6.97}$	$0.18^{+0.15}_{-0.08}$	$0.06^{+0.13}_{-0.15}$	$1.51^{+0.04}_{-0.08}$	$0.30^{+0.14}_{-0.08}$	2.0	inverse (age) inside-out (metallicity)

Note. (1) Name of the model as introduced in the main text. (2) Additional constraints on the age and metallicity of the two SSPs. (3) Inferred age of the central SSPs (here and in the following, we quote the median value of the marginalized posterior distribution; the uncertainties refer to the 16 and 84th percentile of the probability). (4) Inferred age of the outer SSP. (5) Inferred metallicity of the central SSP. (6) Inferred metallicity of the outer SSP. (7) Inferred value of the concentration parameter. (8) Inferred value of the mass fraction of the central SSP in the central pixel. (9) χ^2 per degree of freedom. (10) Description of the model outcome: 'inverse' refers to positive radial gradients in age and/or metallicity, and 'inside-out' refers to negative radial gradients in age and/or metallicity.

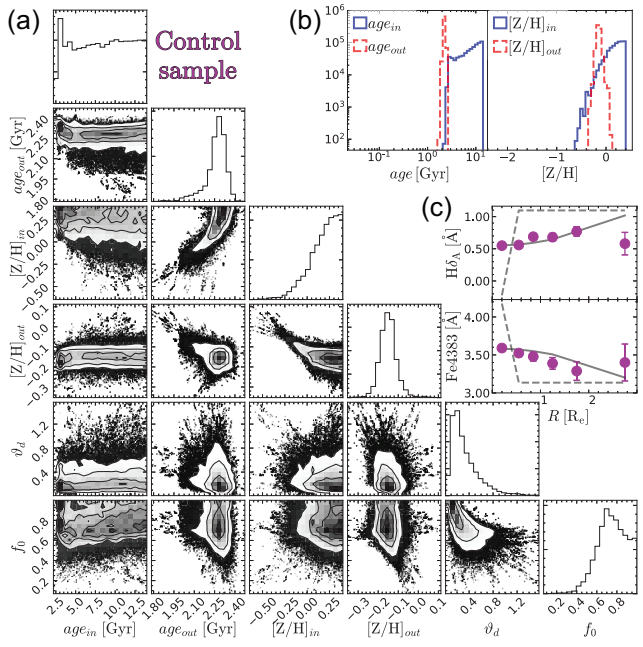

Figure 6. Our two-SSP toy model requires inside-out age and/or metallicity gradients for the control sample of quiescent, non-PSB galaxies (panels a and b). The inferred model reproduces the median observed gradients in both H δ_A and Fe 4383 (panel c; the dashed/solid lines show the model prediction before/after seeing convolution, and the magenta circles trace the median index values for our control sample). Even though the age of the inner SSP is poorly constrained, it is clear that $age_{in} > age_{out}$ (panel b): the inner SSP (solid blue histogram) is clearly older than the outer SSP (dashed red histogram, $P < 3 \times 10^{-4}$). In contrast, even though $[Z/H]_{in} > [Z/H]_{out}$, the two SSP metallicities are consistent within the uncertainties ($P < 0.07$). Notice the strong degeneracy between the parameters of the two SSPs.

Panel (b) shows the age and metallicity histograms of the two SSPs: Unlike for PSB galaxies, here the central SSP (solid blue histogram) has both older age and higher metallicity than the outer SSP. We find $age_{in} = 8.3^{+3.9}_{-4.2}$ Gyr whereas $age_{out} = 2.27^{+0.08}_{-0.05}$ Gyr; for metallicity, the results are $[Z/H]_{in} = 0.21^{+0.13}_{-0.19}$ and $[Z/H]_{out} = -0.15^{+0.04}_{-0.04}$. For control galaxies, the probability that the two ages are the same is $P < 3 \times 10^{-4}$ (using the joint posterior probability distribution of age_{in} and age_{out}).[5] It is unclear whether and to what extent this sharp cut-off might be caused by our stacking analysis. In fact, on one hand, the youngest galaxies are (on average) the smallest, which enhances their contribution to the innermost radial bins and biases age_{in} to younger values; on the other hand, however, the oldest galaxies, despite being on average the largest, tend to have the steepest light profiles, which also enhances their contribution to the innermost bins. Disentangling these two competing effects is, however, beyond the scope of this paper. From Fig. 6(b), we also notice that SSP age for both the inner and outer SSPs is larger than that in PSB galaxies. This might be due either to the different mass distribution of the two samples, but also to problems inherent with the stacking analysis. For example, if the youngest PSB galaxies are also the most compact, their PSF would be larger than the median PSF (when expressed in units of R_e), causing more contamination between the inner and outer SSPs. In light of this ambiguity, we do not overinterpret the observed age difference between control galaxies and the outer SSP of PSB galaxies. For metallicity, we find $[Z/H]_{in} > [Z/H]_{out}$, but this result is not statistically significant (the probability that the two SSPs have the same metallicity is $P < 0.07$).

At face value, however, we find that modelling the control sample requires the central SSP to be older and more metal rich than the outer SSP, as observed in most local quiescent galaxies (e.g. McDermid et al. 2015; Ferreras et al. 2019; Zibetti et al. 2020) and at variance with the model for PSB galaxies.

4.3 Constrained PSB models

Could an inside-out SSP gradient reproduce the observed radial trends of H δ_A and Fe 4383 for PSB galaxies? We have already shown that the benchmark model points to an inverse age structure for PSB galaxies; therefore, we know that an inside-out structure is less likely. However, our two-SSP model has only six degrees of freedom; therefore, its predictive power is modest. For this

[5] In this case, assuming a Gaussian probability with standard deviation equal to the standard deviation of the posterior yields $P < 0.1$, but this estimate is too conservative: The large difference in probability between the two estimates arises from the shape of the posterior probability distribution of age_{in}, which has a sharp cut-off below ≈2.5 Gyr (Fig. 6a).

reason, it is important to evaluate directly how much worse an inside-out model would be relative to the benchmark model. To address this question, we create two more PSB models, identical to the benchmark model, but constrained to have inside-out age or metallicity gradients. The first model has free age but $[Z/H]_{in} > [Z/H]_{out}$ (PSB inside-out metallicity model, Table 1). For this model, we find that $age_{in} < age_{out}$, consistent with the benchmark model; the fact that – by construction – $[Z/H]_{in} > [Z/H]_{out}$ yields a marginally higher $\chi^2_\nu = 2.0$ compared to the benchmark $\chi^2_\nu = 1.9$. The second model has free metallicity, but $age_{in} > age_{out}$ (PSB inside-out age model, Table 1). The best-fitting parameters for this model predict flat $H\,\delta_A$ and Fe 4383 radial profiles, inconsistent with observations. Quantitatively, the reduced $\chi^2_\nu \approx 6$ is larger than the value for the fiducial model ($\chi^2_\nu = 1.9$). We conclude that an inside-out age structure is inconsistent with the radial variations of $H\,\delta_A$ and Fe 4383 observed for the stacked PSB galaxies. These two constrained models suggest that, while inside-out age gradients are ruled out for the PSB sample, both inside-out and inverse metallicity gradients are consistent with observations (cf. Cresci et al. 2010; Schönrich & McMillan 2017).

4.4 Effect of extended SFH

While an SSP is a good model for a starburst (where the spread in stellar age is narrow by definition), stellar populations are known to have extended SFHs. To what extent the different properties of SSPs and more realistic stellar population might bias our results? To address this question, we implemented a three-SSP model. For brevity, we refer to these SSPs by increasing roman numerals I–III. In order to preserve some predictive power, we want the smallest possible number of free parameters. For this reason, the three SSPs have different ages (age_I, age_{II}, and age_{III}) but equal metallicity [Z/H]. Even though this restriction is not realistic, it reflects the fact that, with our two indices, we do not find strong metallicity differences within the PSB sample (right-hand panel of Fig. 4b). For the radial variation, we use the same parametrization introduced for the benchmark model (equation 1; again, like we did for the benchmark model, we parametrize R_d as $\tan\vartheta_d$, with $0 \leq \vartheta_d \leq \pi/2$). Using the same parametrization means that SSP I can be safely interpreted as the inner SSP from the benchmark model, whereas the outer SSP from the benchmark model corresponds here to the superposition of SSP II and SSP III: This superposition is the zero-order approximation for an extended SFH. At any radius R, the values of the mass fractions are $f_I(R)$, $f_{II}(R)$, and $f_{III}(R)$, which we parametrize using two variables $0 \leq \vartheta \leq \pi/2$ and $0 \leq \varphi \leq \pi/2$:

$$\begin{cases} f_I(R) \equiv & \cos^2(\vartheta)\, f(R) \\ f_{II}(R) \equiv & [1 - \cos^2(\vartheta)\, f(R)]\, \cos^2(\varphi) \\ f_{III}(R) \equiv & [1 - \cos^2(\vartheta)\, f(R)]\, \sin^2(\varphi). \end{cases} \quad (2)$$

It can be easily verified that these functions express meaningful fractions, because they satisfy both $f_I(R) + f_{II}(R) + f_{III}(R) = 1$ and $0 \leq f_x(R) \leq 1; \forall x \in \{I, II, III\}$. In particular, the angle ϑ expresses the fraction of SSP I at $R = 0$, via $f_I(0) = \cos^2(\vartheta)$, whereas the angle φ expresses the fraction, relative to the *remaining* stellar population, of SSP II (resp. SSP III) via $\cos^2(\varphi)$ [resp. $\sin^2(\varphi)$]. Notice that the fraction of SSP II decreases with increasing φ, whereas the fraction of SSP III increases with increasing φ. This model has an undesired symmetry, in that the results are unchanged swapping (age_{II}, age_{III}, φ) with (age_{III}, age_{II}, $\pi/2 - \varphi$); therefore, we further require $age_{II} \leq age_{III}$ by assigning zero probability to non-complying models. This means that SSP II is always younger than SSP III; therefore, the age of the outer SSP (equal to the sum of SSP II and SSP III) increases with increasing φ. So far, the model has seven free parameters: age_I, age_{II}, age_{III}, [Z/H], ϑ, φ, and ϑ_d. To reduce this number, we further constrain ϑ and ϑ_d to reproduce the corresponding optimal values from the benchmark model, i.e. we set $\vartheta_d = 1.41$ and $\vartheta = \arccos\sqrt{f_0}$, with $f_0 = 0.15$ (first row of Table 1).

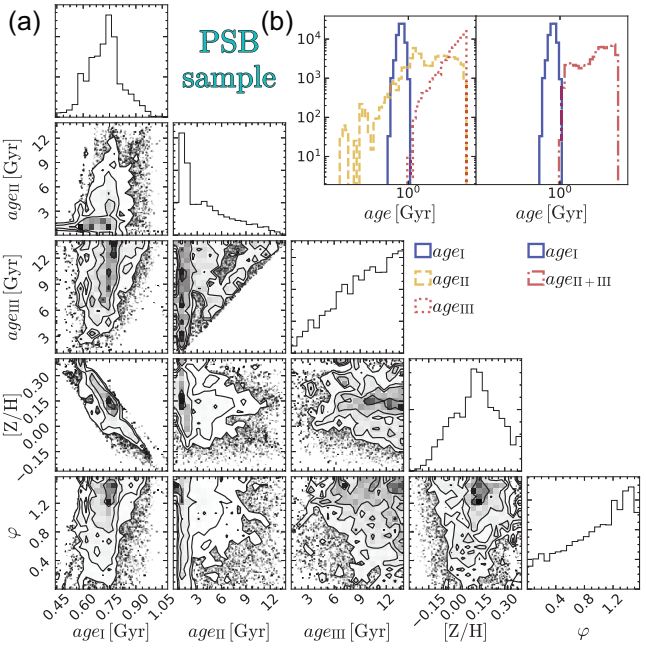

Figure 7. Assessing the effect of extended SFHs instead of SSPs for PSB galaxies. The model uses three SSPs: SSP I corresponds to the inner stellar population, whereas the superposition of the young SSP II and the old SSP III is a first-order approximation to an extended SFH. The corner diagram (panel a) shows that the fraction of SSP III stars ($\cos^2\varphi$) anticorrelates with age_{II} (the age of the younger SSP II) and correlates with age_{III} (the age of the older SSP III). This behaviour reflects the fact that the indices considered here constrain only the average age of the outer stellar population: This value of the age can be attained with both a long SFH or a short SFH. Panel 7b, left, shows the probability distribution of the three SSP ages: age_I (solid blue) is clearly younger than both age_{II} (dashed yellow) and age_{III} (dot–dashed red). Even though occasionally $age_{II} \leq age_I$, this occurs with relatively low probability $P < 0.07$. More importantly, in the right-hand panel we can see that the inner SSP is systematically younger than the outer SSP ($P < 10^{-5}$).

This model reproduces the observed index profiles as well as the benchmark model ($\chi^2_\nu = 10^{1000}$); the marginalized posterior probability is illustrated by the corner diagram in Fig. 7(a). We find the usual age–metallicity degeneracy, between each SSP age and [Z/H] (the Spearman rank correlation coefficients for age_I, age_{II}, and age_{III} are $\rho = -0.81$, -0.21, and -0.10, respectively). φ, the parameter governing the relative fraction of SSP II and SSP III, correlates with age_I ($\rho = 0.30$): This positive correlation reflects the fact that the measured index profiles must be met by diluting a relatively younger/older starburst (SSP I) with a correspondingly younger/older outer SSP (SSP II + SSP III). This implies that our indices constrain only the mean age of the outer population. For this reason, φ anticorrelates with age_{II} ($\rho = -0.16$), because for a given value of age_I and age_{III}, the required age of the outer SSP must be met either with a low fraction of young SSP II stars (larger φ) or with a high fraction of relatively older SSP II stars (lower φ). Similar reasoning explains the positive correlation between φ and age_{III}.

In Fig. 7(b) (left-hand panel), we report the posterior distribution of the three SSPs: It can be seen that SSP II (dashed yellow histogram)

overlaps with SSP III (dotted red histogram), but this does not mean that $age_{II} \geq age_{III}$, as can be seen from the joint probability distribution of age_{II} and age_{III} (third row, second column of the corner diagram, Fig. 7a). It is instead true that SSP II is occasionally younger than SSP I (dashed yellow and solid blue histograms, respectively): this occurs with a probability of $P < 0.07$. However, even these 7 per cent of cases do not contradict the main conclusion that PSB galaxies have inverse age gradients. In fact, what really matters is the mean age of the outer SSP, consisting of both SSP II and the older SSP III. The age of the outer SSP is illustrated in the right-hand panel of Fig. 7(b) (dot–dashed red histogram), where we reproduce again the histogram of age_I for ease of comparison (solid blue line). In no case we find that the outer age is younger than the age_I (the overlap between the two histograms does not take into account the positive correlation between the age of the three SSPs). By comparing this histogram with the left-hand panel of Fig. 5(b), illustrating the results for the benchmark model, we see that the three-SSP model allows for much older outer SSPs than the benchmark model, reflecting the oversimplification of using a single SSP (in the benchmark model) instead of an extended SFH. Thus, in general we can expect older ages for all of our non-starburst components.

5 DISCUSSION

The different mass–size relations of SF and Q galaxies, as well as their evolution with cosmic time, require a link between star formation and structural evolution in galaxies (Section 1). There are several physical processes that can cause an SF galaxy to become quiescent, and each one of them might impart different structural signatures on newly quiescent galaxies. For this reason, we can reasonably expect to learn something about how galaxies become quiescent by studying the structural differences between SF, Q, and newly quiescent galaxies. We can roughly divide quenching mechanisms in two classes, based on their time-scale relative to the visibility time of PSB galaxies, strongly constrained by the lifetime of A-type stars (< 1 Gyr).

Slow quenching processes act over a few Gyr, longer than the typical star formation time-scale at $z = 0.8$ (defined as the typical inverse specific star formation rate $sSFR^{-1} \approx 1$ Gyr; Noeske et al. 2007). These processes include (i) virial shocks (which prevent the accretion of cold gas, but leave the existing gas disc intact; Birnboim & Dekel 2003; Dekel & Birnboim 2006), (ii) radio-mode feedback due to active galactic nuclei[6] (AGN; Croton et al. 2006; Barišić et al. 2017), and (iii) stabilization of the gas disc against fragmentation ($Q-$quenching; Martig et al. 2009; Cacciato, Dekel & Genel 2012; Krumholz & Thompson 2013; Dekel & Burkert 2014; Forbes et al. 2014). These mechanisms cause little or no disruption to the gas that is currently fuelling star formation, so that the galaxy can continue on the SF sequence for some time, until the cold-gas supply is either exhausted or otherwise unable to form stars. By definition, these mechanisms act gradually, thereby leaving a Q galaxy with roughly the same mass and size, and the same structure as the original SF galaxy. Most SF galaxies form in an *inside-out* fashion (Pezzulli et al. 2015; Ellison et al. 2018; Wang et al. 2019), leading to negative age gradients. At the same time, chemical enrichment models predict negative or flat stellar metallicity gradients (with some inversion in the centre; see Schönrich & McMillan 2017). Thus, the fact that our control sample of Q galaxies shows negative age and metallicity gradients (Section 4.2) is qualitatively consistent with the slow quenching and subsequent passive evolution of SF galaxies from earlier epochs, without major structural changes. There are two important caveats to this conclusion. First, our results are derived from stacks, so they are valid only in an average sense: We cannot say whether (or what fraction of) passive galaxies had more complex SFHs, with star formation ending last in the centre, or with later central starbursts (rejuvenation; see Chauke et al. 2018, for an integrated analysis using LEGA-C). Secondly, and more importantly, we remark that control galaxies became quiescent at earlier epochs compared to $z \approx 0.8$ PSB galaxies, at a time when the star formation time-scale was shorter.

On the other hand, fast-quenching processes happen on relatively short time-scales ($\lesssim$1 Gyr; e.g. Kaviraj et al. 2007; Dekel & Burkert 2014), shorter than the time-scale of star formation. These processes involve, in one way or another, the removal of the currently SF gas: through AGN-driven galactic-scale winds (Springel, Di Matteo & Hernquist 2005; Kaviraj et al. 2007; Baron et al. 2018), through ram-pressure stripping (in galaxy clusters; Gunn & Gott 1972),[7] or via rapid gas-consumption in gas-rich mergers (Barnes & Hernquist 1991, 1996; Hopkins et al. 2009; Dekel & Burkert 2014). A key property of the fast-quenching processes is that all of them either require or cause the presence of centrally concentrated cold gas. This gas builds up a dense stellar core, thereby increasing the stellar mass and shrinking the half-light radius of the underlying galaxy just before it becomes quiescent. Some of the fast-quenching mechanisms also produce an increasing age trend with radius (Mihos & Hernquist 1994; Bekki et al. 2005), a signature opposite to the negative age gradients expected from inside-out formation.

5.1 Evidence of central starbursts in PSB galaxies

PSB galaxies are passive galaxies with a significant fraction of young stars. They lack current star formation on time-scales of 10–100 Myr (depending on the tracer used) and they have prominent Balmer spectral features typical of A-type stars, which have lifetimes of < 1 Gyr. These two time-scales constrain the quenching time-scale of PSB galaxies, placing them decisively in the fast-quenching channel. We argue that the structural properties of PSB galaxies are in qualitative agreement with the expectations of the fast-quenching scenario described above.

First, our PSB galaxies show a high merger fraction (0.40) relative to field galaxies (0.16 ± 0.02 at $z \approx 1$; Mantha et al. 2018, their table 2). Given our sample size and assuming Poisson uncertainties, the probability that the PSB sample has the same merger rate as observed in the field is relatively modest ($P = 0.02$). This suggests that gas-rich mergers are an important trigger of PSB evolution, in agreement with the theoretical scenario proposed above. Notice, however, that the value $P = 0.02$ assumes that the merger classification was perfect. In practice, there are two main uncertainties that are hard to quantify in our small sample: Misclassification can bias the P-value to lower values (e.g. asymmetries due to dust and chance alignments misclassified as mergers), whereas uncertainties on the visibility time of merger signatures bias the P-value to higher values. Nevertheless, our results are qualitatively unchanged if we repeat the test separately for merging and non-merging PSBs (Section 3); therefore, it is

[6]but notice that, depending on the angle of the radio jet with respect to the gas disc, radio-mode feedback may lead to molecular outflows (see e.g. García-Burillo et al. 2014; Sakamoto et al. 2014; Morganti et al. 2015; Dasyra et al. 2016).

[7]Given that our sample consists mostly of central/isolated galaxies, we ignore ram-pressure stripping from here on.

unlikely that the high-visibility mergers we are able to discern are the only channel for PSB formation: The remaining 60 per cent of PSB galaxies that show no evidence of major mergers could either: (i) be mergers below our detection threshold (e.g. Zabludoff et al. 1996; Goto 2005; Yang et al. 2008; Pracy et al. 2009 find merger fractions between 15 and 70 per cent, depending on sample selection and image quality; see Pawlik et al. 2018, for a discussion), or (ii) have accreted low-stellar-mass, gas-rich satellites, or (iii) have undergone a qualitatively different mode of gas accretion, such as cold flows (Dekel et al. 2009). Regardless, all of these channels are consistent with the fast-quenching scenario. This high but not overwhelming merger fraction is consistent with the prediction of cosmological *N*-body simulations, which suggests that roughly half of PSB galaxies did not experience a recent merger (Wilkinson et al. 2018; Davis et al. 2019; Pawlik et al. 2019).

Secondly, stacking analysis of $z > 1$ PSB galaxies show evidence of high-velocity outflows (Maltby et al. 2019), capable of removing the SF gas and thus halting star formation abruptly. There is at least one case where this process has been observed in act (Baron et al. 2018). These outflows may temporarily delay star formation, until other physical processes, acting on longer time-scales, can permanently halt the supply of cold gas and make the galaxy quiescent.

Moreover, the structural changes expected from fast quenching go in the right direction *vis-à-vis* the observed differences between normal and PSB galaxies on the mass–size plane: At a given stellar mass, PSB galaxies are slightly smaller than normal Q galaxies and are much smaller than SF galaxies (Whitaker et al. 2012; Yano et al. 2016; Wu et al. 2018).

Finally, in this work we provide direct evidence that PSB galaxies at $z \approx 0.8$ have younger stellar populations in their centres, thereby demonstrating that, in these galaxies, star formation occurred last in the centre. This event is different from the typical inside-out formation that characterizes both the control sample (Fig. 4, magenta) as well as the bulk of local SF galaxies (e.g. González Delgado et al. 2015; Zibetti et al. 2017; Ellison et al. 2018).

5.2 The progenitors of PSB galaxies

The discovery that PSB galaxies have inverse stellar population gradients is in agreement with the hypothesis that PSB galaxies are descendants of compact star-forming (CSF) galaxies. These galaxies are characterized by high star formation rates and small size relative to SF galaxies of the same mass (star formation rate $> 100\,\mathrm{M}_\odot\,\mathrm{yr}^{-1}$, $R_\mathrm{e} < 3$ kpc; e.g. Barro et al. 2013, 2014; van Dokkum et al. 2015). Yet this high star formation rate is mostly undetected in the rest-frame optical wavelengths because it is obscured by large optical depth.

Even though the number density of CSF galaxies is too high compared to that of PSB galaxies (Wild et al. 2016), CSF galaxies are not guaranteed to become quiescent; hence, their number density does not need to match exactly that of PSB galaxies. For example, CSF galaxies could transition to a state of lowered star formation rate instead of becoming quiescent.

On the other hand, there is evidence that CSF galaxies, too, have inverse stellar population gradients, because their star formation is less extended than the already-formed stellar population (Barro et al. 2016, 2017; Popping et al. 2017; Tadaki et al. 2017). If CSF galaxies transitioned to a relatively long phase of lowered star formation rate, characterized by inside-out growth, the inverse signature on their stellar populations might be erased (at least in part, giving rise to U-shaped age profiles observed in some local early-type galaxies; Zibetti et al. 2020). If at least some of these galaxies were about to undergo a rapid cessation of star formation, the inverse gradients would be 'frozen'. Our finding that PSB galaxies harbour inverse stellar population gradients agrees with the hypothesis that at least some of their progenitors might be CSF galaxies that underwent rapid quenching.

Alternatively, the progenitors of PSB galaxies could be galaxies detected at sub-mm wavelength (sub-mm galaxies; Smail, Ivison & Blain 1997; Barger et al. 1998; Hughes et al. 1998; Eales et al. 1999). These galaxies are characterized by high star formation rates (Swinbank et al. 2014), consistent with the SFH of PSB galaxies (Wild et al. 2020). Moreover, the combination of the number density of sub-mm galaxies (≈6 times higher than that of PSB; Simpson et al. 2014; Swinbank et al. 2014) and the visibility time of the sub-mm phase (≈6 times shorter than that of PSB; Hainline et al. 2011; Hickox et al. 2012) cancels out and matches the observed number density of observed PSB galaxies (Wild et al. 2020).

5.3 Caveats

Given our sample selection criteria, it is difficult to assess the generality of our results *vis-á-vis* the unbiased population of PSB galaxies at a redshift of $z \approx 0.8$. In fact, our SNR and spatial resolution bias the sample towards the largest and brightest PSB galaxies; therefore, a trend between stellar-population gradients and size or luminosity could mean that our conclusions are not representative of the whole PSB population. Conversely, removing galaxies with small R_e means that our sample is biased against the most compact PSB galaxies, which may represent the youngest galaxies in this category (Wu et al. 2020). For these reasons, we cannot draw stringent conclusions concerning how size affects the properties of our galaxies (but we remark that jackknifing our sample about the median R_e yields consistent results for the smallest and largest PSBs considered here). However, we can still robustly conclude that inverse age gradients are representative of ≈50 per cent of the PSB population (even though individual PSB galaxies can indeed have inside-out gradients, e.g. 258467 has a positive $\mathrm{H}\,\delta_\mathrm{A}$ gradient with four standard deviations; see also Appendix B and Hunt et al. 2018). Moreover, our data suggest that, provided the galaxies are at least partially resolved, there is no strong dependence of the incidence of inverse gradients with either galaxy size or galaxy concentration. Finally, we find that our results cannot be explained by environment effects (i.e. ram-pressure stripping), because the inverse gradients persist for only central/isolated galaxies.

Using the UVJ diagram to select Q galaxies may bias our sample, by including misclassified SF galaxies. There are two indications that this is not the case. First, if we select only PSB galaxies where the wavelength range includes rest-frame $\mathrm{H}\,\beta$, and if for these galaxies we further require an equivalent width of $\mathrm{EW}(\mathrm{H}\,\beta) \geq 1$ Å, we still find inverse gradients for $\mathrm{H}\,\delta_\mathrm{A}$ (emission lines have a negative EW). For Fe 4383, the gradients are consistent with being flat, but this is likely due to the smaller sample size. Secondly, a preliminary analysis of SF galaxies finds inside-out gradients, similar to non-PSB quiescent galaxies; therefore, any contamination would make our results weaker.

Another caveat is that, at least for PSB galaxies, the SNR of $\mathrm{H}\,\delta_\mathrm{A}$ is higher than the SNR of Fe 4383 , which might skew our analysis. Furthermore, we are unable to constrain the abundance of α-elements relative to Fe, which is important to properly constrain the metallicity of a stellar population (e.g. González 1993; Thomas, Maraston & Bender 2003; Conroy 2013), We note though that this should not be a concern for determining the age of the PSB galaxies (Leonardi & Rose 1996), but might affect the older control sample.

Unfortunately, at present we cannot derive strong quantitative constraints on the stellar population gradients in PSB galaxies: Seeing convolution prevents us from breaking the degeneracy between spatial distribution, age, and mass fraction of the young, central subpopulation. Still, the observed agreement with local observations is promising (Section 4.1). In addition, the need for stacking data from different galaxies means that our models do not necessarily capture the unbiased average of the population. Individual galaxies show a plethora of radial behaviours, as suggested by resolved studies of individual galaxies in the local Universe (e.g. Pracy et al. 2013; Chen et al. 2019; Owers et al. 2019): The fact that some PSB galaxies have flat gradients is not in contradiction with our results. These different radial behaviours may depend on the timing and on the properties of the burst.

5.4 Future work

Current observing facilities are unable to disentangle this degeneracy; therefore, we foresee a multipronged approach.

Space-based observations have enough spatial resolution to resolve the inner structure of PSB galaxies. Unfortunately, at the time of this writing, the number of PSB galaxies with adequate photometry in two bands is limited, and cannot be used to draw strong conclusions for our sample (Appendix B). At variance with our findings, Maltby et al. (2018) find no evidence of colour gradients in a sample of 80 PSB galaxies at $0.5 < z < 2$, but they rely on photometry only; therefore, a direct comparison is not warranted.

Another implication of the scenario proposed is that the youngest PSB galaxies ought to have the smallest half-light radii. This is because the younger central population has a lower mass-to-light ratio, but dims faster than the older, extended population (as indeed confirmed by Wu et al. 2020; see their discussion for the effect of dust).

Studying the structure of local galaxies is complicated by the intervening evolution between $z \approx 0.8$ and now, but inverse age structures have been found in the most massive early-type galaxies (Zibetti et al. 2020). This approach should be combined with a study of starburst dwarf galaxies in the local Universe. These systems have many properties in common with higher mass galaxies in the early Universe (e.g. Lelli, Verheijen & Fraternali 2014; Yang et al. 2017). Intriguingly, some of these local galaxies have inverse age structures caught in formation (Zhang et al. 2012), and might shed light on the physical processes occurring at high gas fractions.

Accurate modelling involving more than indices (e.g. Zibetti et al. 2017) may also provide more stringent constraints on the age and metallicity of PSB galaxies, resolving some of the degeneracies inherent to using only two indices (Section 4.1). The upcoming third data release of LEGA-C will likely improve both the precision and the accuracy of our measurements. Moreover, owing to a larger sample and thanks to the improved sky subtraction at the reddest wavelengths, it will unlock additional stellar-population information.

6 SUMMARY

We have used a sample of 17 UVJ-colour selected, spectrally confirmed PSB galaxies from the deep, $z \approx 0.8$ LEGA-C Survey, to study the radial variation of the strength of the H δ_A and Fe 4383 absorption indices. We find that

(i) PSB galaxies show negative H δ_A radial gradients and positive Fe 4383 gradients (P-values 10^{-4} and 0.04, respectively).

(ii) The control sample of quiescent, non-PSB galaxies, selected to match the mass range of the PSB sample, presents positive H δ_A radial gradients and negative Fe 4383 radial gradients (P-values 0.07 and 0.02, respectively).

(iii) These trends imply a positive (inverse) age gradient with radius for PSB galaxies, and a negative age and/or metallicity gradient for control quiescent galaxies (the control sample).

(iv) Coupled with the mass and size distribution of PSB and quiescent galaxies, and with the higher than average merger fraction (0.4), our data suggest that PSB galaxies have undergone a central starburst, which decreased their effective radius and possibly caused them to become quiescent on a fast time-scale (< 1 Gyr).

ACKNOWLEDGEMENTS

We thank the anonymous referee for helpful comments and suggestions. Based on observations made with ESO Telescopes at the La Silla Paranal Observatory under programme ID 194-A.2005 (The LEGA-C Public Spectroscopy Survey). This project has received funding from the European Research Council (ERC) under the European Union's Horizon 2020 research and innovation programme (grant agreement no. 683184). We are grateful to N. Scott for sharing the spectral fitting code. PFW acknowledges the support of the East Asian Core Observatories Association fellowship. TMB is supported by an Australian Government Research Training Program Scholarship. AG and SZ acknowledge support from Istituto Nazionale di Astrofisica (PRIN-SKA2017 program 1.05.01.88.04).

This work made extensive use of the Debian GNU/Linux operative system, freely available at http://www.debian.org. We used the Python programming language (van Rossum 1995), maintained and distributed by the Python Software Foundation, and freely available at http://www.python.org. We acknowledge the use of SCIPY (Jones et al. 2001), MATPLOTLIB (Hunter 2007), EMCEE (Foreman-Mackey et al. 2013), ASTROPY (Astropy Collaboration 2013), and PATHOS (McKerns et al. 2011). During the preliminary analysis, we have made extensive use of TOPCAT (Taylor 2005).

DATA AVAILABILITY

The raw data used in this work are available in the public domain, through the ESO Science Archive and through the Mikulski Archive for Space Telescopes (MAST). Part of the reduced data has been released with the second public data release of LEGA-C (Straatman et al. 2018), available on the LEGA-C website. Resolved measurements will be available in the upcoming third public data release of LEGA-C.

REFERENCES

Almaini O. et al., 2017, MNRAS, 472, 1401
Astropy Collaboration, 2013, A&A, 558, A33
Balogh M. L., Morris S. L., Yee H. K. C., Carlberg R. G., Ellingson E., 1997, ApJ, 488, L75
Balogh M. L., Morris S. L., Yee H. K. C., Carlberg R. G., Ellingson E., 1999, ApJ, 527, 54
Barger A. J., Cowie L. L., Sanders D. B., Fulton E., Taniguchi Y., Sato Y., Kawara K., Okuda H., 1998, Nature, 394, 248
Barišić I. et al., 2017, ApJ, 847, 72
Barnes J. E., Hernquist L., 1996, ApJ, 471, 115
Barnes J. E., Hernquist L. E., 1991, ApJ, 370, L65
Baron D. et al., 2018, MNRAS, 480, 3993
Barone T. M., D'Eugenio F., Colless M., Scott N., 2020, preprint (arXiv: 2006.00720)

Barro G. et al., 2013, ApJ, 765, 104
Barro G. et al., 2014, ApJ, 791, 52
Barro G. et al., 2016, ApJ, 827, L32
Barro G. et al., 2017, ApJ, 851, L40
Bekki K., Shioya Y., Couch W. J., 2001, ApJ, 547, L17
Bekki K., Couch W. J., Shioya Y., Vazdekis A., 2005, MNRAS, 359, 949
Belli S., Newman A. B., Ellis R. S., 2017, ApJ, 834, 18
Bertelli G., Nasi E., Girardi L., Marigo P., 2009, A&A, 508, 355
Bezanson R. et al., 2018, ApJ, 858, 60
Birnboim Y., Dekel A., 2003, MNRAS, 345, 349
Buck T., Obreja A., Macciò A. V., Minchev I., Dutton A. A., Ostriker J. P., 2020, MNRAS, 491, 3461
Cacciato M., Dekel A., Genel S., 2012, MNRAS, 421, 818
Cappellari M. et al., 2013, MNRAS, 432, 1709
Cappellari M., Emsellem E., 2004, PASP, 116, 138
Carlberg R. G., Morris S. L., Yee H. K. C., Ellingson E., 1997, ApJ, 479, L19
Chabrier G., 2003, PASP, 115, 763
Chauke P. et al., 2018, ApJ, 861, 13
Chen Y.-M. et al., 2019, MNRAS, 489, 5709
Conroy C., 2013, ARA&A, 51, 393
Couch W. J., Sharples R. M., 1987, MNRAS, 229, 423
Cresci G., Mannucci F., Maiolino R., Marconi A., Gnerucci A., Magrini L., 2010, Nature, 467, 811
Croton D. J. et al., 2006, MNRAS, 365, 11
Darvish B., Mobasher B., Martin D. C., Sobral D., Scoville N., Stroe A., Hemmati S., Kartaltepe J., 2017, ApJ, 837, 16
Dasyra K. M., Combes F., Oosterloo T., Oonk J. B. R., Morganti R., Salomé P., Vlahakis N., 2016, A&A, 595, L7
Davis T. A., van de Voort F., Rowlands K., McAlpine S., Wild V., Crain R. A., 2019, MNRAS, 484, 2447
Dekel A., Birnboim Y., 2006, MNRAS, 368, 2
Dekel A., Burkert A., 2014, MNRAS, 438, 1870
Dekel A. et al., 2009, Nature, 457, 451
Dressler A., Gunn J. E., 1983, ApJ, 270, 7
Dressler A., Smail I., Poggianti B. M., Butcher H., Couch W. J., Ellis R. S., Oemler Augustus J., 1999, ApJS, 122, 51
Eales S., Lilly S., Gear W., Dunne L., Bond J. R., Hammer F., Le Fèvre O., Crampton D., 1999, ApJ, 515, 518
Ellison S. L., Sánchez S. F., Ibarra-Medel H., Antonio B., Mendel J. T., Barrera-Ballesteros J., 2018, MNRAS, 474, 2039
Fagioli M., Carollo C. M., Renzini A., Lilly S. J., Onodera M., Tacchella S., 2016, ApJ, 831, 173
Falcón-Barroso J., Sánchez-Blázquez P., Vazdekis A., Ricciardelli E., Cardiel N., Cenarro A. J., Gorgas J., Peletier R. F., 2011, A&A, 532, A95
Ferreras I. et al., 2019, MNRAS, 489, 608
Forbes J. C., Krumholz M. R., Burkert A., Dekel A., 2014, MNRAS, 438, 1552
Foreman-Mackey D., Hogg D. W., Lang D., Goodman J., 2013, PASP, 125, 306
García-Burillo S. et al., 2014, A&A, 567, A125
González J. J., 1993, PhD thesis
González Delgado R. M. et al., 2015, A&A, 581, A103
Goto T., 2005, MNRAS, 357, 937
Grogin N. A. et al., 2011, ApJS, 197, 35
Gunn J. E., Gott J. R., III, 1972, ApJ, 176, 1
Hainline L. J., Blain A. W., Smail I., Alexand er D. M., Armus L., Chapman S. C., Ivison R. J., 2011, ApJ, 740, 96
Hickox R. C. et al., 2012, MNRAS, 421, 284
Hiner K. D., Canalizo G., 2015, ApJ, 799, 59
Hopkins P. F., Cox T. J., Dutta S. N., Hernquist L., Kormendy J., Lauer T. R., 2009, ApJS, 181, 135
Hughes D. H. et al., 1998, Nature, 394, 241
Hunt Q. et al., 2018, ApJ, 860, L18
Hunter J. D., 2007, Comput. Sci. Eng., 9, 90
Jones E. et al., 2001, SciPy: Open Source Scientific Tools for Python. http://www.scipy.org/
Kauffmann G. et al., 2003, MNRAS, 341, 33
Kaviraj S., Kirkby L. A., Silk J., Sarzi M., 2007, MNRAS, 382, 960
Koekemoer A. M. et al., 2007, ApJS, 172, 196
Krumholz M. R., Thompson T. A., 2013, MNRAS, 434, 2329
La Barbera F., Ferreras I., de Carvalho R. R., Bruzual G., Charlot S., Pasquali A., Merlin E., 2012, MNRAS, 426, 2300
Labbé I. et al., 2005, ApJ, 624, L81
Le Fèvre O. et al., 2003, in Iye M., Moorwood A. F. M., eds, Proc. SPIE Conf. Ser. Vol. 4841, Instrument Design and Performance for Optical/Infrared Ground-Based Telescopes. SPIE, Bellingham, p. 1670
Lelli F., Verheijen M., Fraternali F., 2014, A&A, 566, A71
Leonardi A. J., Rose J. A., 1996, AJ, 111, 182
Maltby D. T., Almaini O., Wild V., Hatch N. A., Hartley W. G., Simpson C., Rowlands K., Socolovsky M., 2018, MNRAS, 480, 381
Maltby D. T. et al., 2019, MNRAS, 489, 1139
Mantha K. B. et al., 2018, MNRAS, 475, 1549
Martig M., Bournaud F., Teyssier R., Dekel A., 2009, ApJ, 707, 250
Martig M., Minchev I., Ness M., Fouesneau M., Rix H.-W., 2016, ApJ, 831, 139
Martín-Navarro I., Vazdekis A., Falcón-Barroso J., La Barbera F., Yıldırım A., van de Ven G., 2018, MNRAS, 475, 3700
Martins L. P., Coelho P., 2007, MNRAS, 381, 1329
McDermid R. M. et al., 2015, MNRAS, 448, 3484
McKerns M. M., Strand L., Sullivan T., Fang A., Aivazis M. A. G., 2011, in van der Walt S., Millman J., eds, Proc. 10th Python in Sci. Conf., Building a Framework for Predictive Science. Austin, Texas, p. 76
Metropolis N., Rosenbluth A. W., Rosenbluth M. N., Teller A. H., Teller E., 1953, J. Chem. Phys., 21, 1087
Mihos J. C., Hernquist L., 1994, ApJ, 427, 112
Morganti R., Oosterloo T., Oonk J. B. R., Frieswijk W., Tadhunter C., 2015, A&A, 580, A1
Mowla L. A. et al., 2019, ApJ, 880, 57
Muzzin A. et al., 2012, ApJ, 746, 188
Muzzin A. et al., 2013, ApJS, 206, 8
Nelson E. J. et al., 2016, ApJ, 828, 27
Noeske K. G. et al., 2007, ApJ, 660, L43
Norton S. A., Gebhardt K., Zabludoff A. I., Zaritsky D., 2001, ApJ, 557, 150
Oke J. B., Gunn J. E., 1983, ApJ, 266, 713
Owers M. S. et al., 2019, ApJ, 873, 52
Paccagnella A., Vulcani B., Poggianti B. M., Moretti A., Fritz J., Gullieuszik M., Fasano G., 2019, MNRAS, 482, 881
Paulino-Afonso A., Sobral D., Buitrago F., Afonso J., 2017, MNRAS, 465, 2717
Pawlik M. M. et al., 2018, MNRAS, 477, 1708
Pawlik M. M., McAlpine S., Trayford J. W., Wild V., Bower R., Crain R. A., Schaller M., Schaye J., 2019, Nat. Astron., 3, 440
Peng C. Y., Ho L. C., Impey C. D., Rix H.-W., 2010, AJ, 139, 2097
Pezzulli G., Fraternali F., Boissier S., Muñoz-Mateos J. C., 2015, MNRAS, 451, 2324
Pietrinferni A., Cassisi S., Salaris M., Castelli F., 2004, ApJ, 612, 168
Pietrinferni A., Cassisi S., Salaris M., Castelli F., 2006, ApJ, 642, 797
Plez B., 2011, J. Phys.: Conf. Ser., 328, 012005
Poci A., McDermid R. M., Zhu L., van de Ven G., 2019, MNRAS, 487, 3776
Poggianti B. M., Smail I., Dressler A., Couch W. J., Barger A. J., Butcher H., Ellis R. S., Oemler Augustus J., 1999, ApJ, 518, 576
Poggianti B. M. et al., 2009, ApJ, 693, 112
Popping G. et al., 2017, A&A, 602, A11
Pracy M. B., Kuntschner H., Couch W. J., Blake C., Bekki K., Briggs F., 2009, MNRAS, 396, 1349
Pracy M. B. et al., 2013, MNRAS, 432, 3131
Prugniel P., Soubiran C., 2001, A&A, 369, 1048
Rousseeuw P. J., Driessen K., 2006, Data Min. Knowl. Discovery, 12, 29
Rowlands K. et al., 2018, MNRAS, 473, 1168
Sakamoto K., Aalto S., Combes F., Evans A., Peck A., 2014, ApJ, 797, 90
Sánchez-Blázquez P. et al., 2006, MNRAS, 371, 703
Schönrich R., McMillan P. J., 2017, MNRAS, 467, 1154
Scott N. et al., 2017, MNRAS, 472, 2833
Scoville N. et al., 2007, ApJS, 172, 38

Serra P., Trager S. C., 2007, MNRAS, 374, 769
Shen S., Mo H. J., White S. D. M., Blanton M. R., Kauffmann G., Voges W., Brinkmann J., Csabai I., 2003, MNRAS, 343, 978
Simpson J. M. et al., 2014, ApJ, 788, 125
Smail I., Ivison R. J., Blain A. W., 1997, ApJ, 490, L5
Springel V., Di Matteo T., Hernquist L., 2005, ApJ, 620, L79
Straatman C. M. S. et al., 2018, ApJS, 239, 27
Suzuki T. L., Minowa Y., Koyama Y., Kodama T., Hayashi M., Shimakawa R., Tanaka I., Tadaki K.-i., 2019, PASJ, 71, 69
Swinbank A. M. et al., 2014, MNRAS, 438, 1267
Tadaki K.-i. et al., 2017, ApJ, 841, L25
Taylor M. B., 2005, in Shopbell P., Britton M., Ebert R., eds, ASP Conf. Ser. Vol. 347, Astronomical Data Analysis Software and Systems XIV. Astron. Soc. Pac., San Francisco, p. 29
Thomas D., Maraston C., Bender R., 2003, MNRAS, 339, 897
Trager S. C., Worthey G., Faber S. M., Burstein D., González J. J., 1998, ApJS, 116, 1
Tran K.-V. H., Franx M., Illingworth G. D., van Dokkum P., Kelson D. D., Magee D., 2004, ApJ, 609, 683
Valenti E., Zoccali M., Renzini A., Brown T. M., Gonzalez O. A., Minniti D., Debattista V. P., Mayer L., 2013, A&A, 559, A98
van de Sande J. et al., 2017, ApJ, 835, 104
van der Wel A., Bell E. F., van den Bosch F. C., Gallazzi A., Rix H.-W., 2009, ApJ, 698, 1232
van der Wel A. et al., 2012, ApJS, 203, 24
van der Wel A. et al., 2014, ApJ, 788, 28
van der Wel A. et al., 2016, ApJS, 223, 29
van Dokkum P. G. et al., 2015, ApJ, 813, 23
van Rossum G., 1995, Python Tutorial, CWI Technical Report CS-R9526. Amsterdam, the Netherlands
Vazdekis A. et al., 2015, MNRAS, 449, 1177
Vazdekis A., Sánchez-Blázquez P., Falcón-Barroso J., Cenarro A. J., Beasley M. A., Cardiel N., Gorgas J., Peletier R. F., 2010, MNRAS, 404, 1639
Wang E., Lilly S. J., Pezzulli G., Matthee J., 2019, ApJ, 877, 132
Whitaker K. E., Kriek M., van Dokkum P. G., Bezanson R., Brammer G., Franx M., Labbé I., 2012, ApJ, 745, 179
Wild V., Walcher C. J., Johansson P. H., Tresse L., Charlot S., Pollo A., Le Fèvre O., de Ravel L., 2009, MNRAS, 395, 144
Wild V., Almaini O., Dunlop J., Simpson C., Rowlands K., Bowler R., Maltby D., McLure R., 2016, MNRAS, 463, 832
Wild V. et al., 2020, MNRAS, 494, 529
Wilkinson C. L., Pimbblet K. A., Stott J. P., Few C. G., Gibson B. K., 2018, MNRAS, 479, 758
Williams C. C. et al., 2017, ApJ, 838, 94
Worthey G., 1994, ApJS, 95, 107
Worthey G., Ottaviani D. L., 1997, ApJS, 111, 377
Wu P.-F. et al., 2018, ApJ, 868, 37
Wu P.-F. et al., 2020, ApJ, 888, 77
Yang Y., Zabludoff A. I., Zaritsky D., Lauer T. R., Mihos J. C., 2004, ApJ, 607, 258
Yang Y., Zabludoff A. I., Zaritsky D., Mihos J. C., 2008, ApJ, 688, 945
Yang H., Malhotra S., Rhoads J. E., Wang J., 2017, ApJ, 847, 38
Yano M., Kriek M., van der Wel A., Whitaker K. E., 2016, ApJ, 817, L21
Younger J. D., Bahcall N. A., Bode P., 2005, ApJ, 622, 1
Zabludoff A. I., Zaritsky D., Lin H., Tucker D., Hashimoto Y., Shectman S. A., Oemler A., Kirshner R. P., 1996, ApJ, 466, 104
Zhang H.-X., Hunter D. A., Elmegreen B. G., Gao Y., Schruba A., 2012, AJ, 143, 47
Zibetti S. et al., 2017, MNRAS, 468, 1902
Zibetti S., Gallazzi A. R., Hirschmann M., Consolandi G., Falcón-Barroso J., van de Ven G., Lyubenova M., 2020, MNRAS, 491, 3562

APPENDIX A: H γ_A AND D_N4000 INDICES

The PSB and control sample have qualitatively different radial trends also in their D_n4000 and H γ_A indices (Fig. A1).

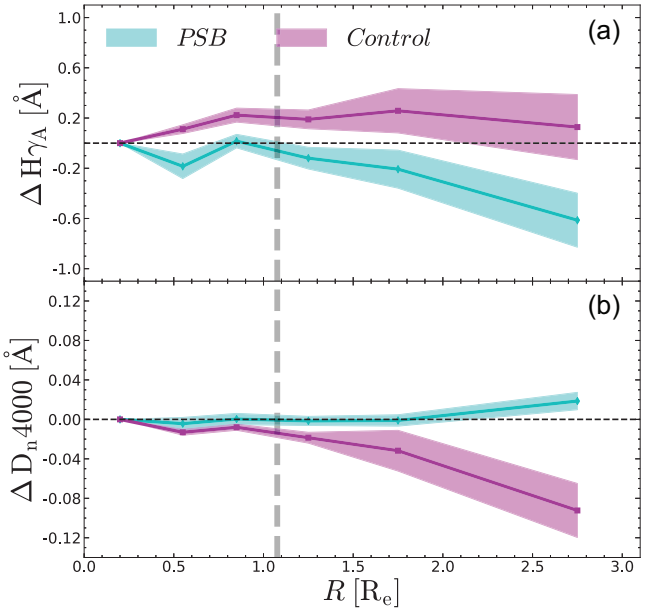

Figure A1. Same as Fig. 4, but for H γ_A (panel A1a) and D_n4000 (panel A1b). These two indices show again that PSB galaxies (cyan) have different radial profiles than the control sample of quiescent, non-PSB galaxies (magenta). For PSB galaxies, H γ_A is radially decreasing and D_n4000 is flat, whereas for control galaxies, H γ_A is radially increasing and D_n4000 is radially decreasing.

APPENDIX B: COLOUR GRADIENTS

Depending on the strength of the intrinsic age gradient, the presence of inverse stellar gradients in PSB galaxies can be investigated using space-based photometry. For a meaningful test, we require two conditions: First, we need space-based photometry to derive intrinsic radial profiles of rest-frame optical colour. Secondly, we need to compare these radial colour profiles to the index profiles of the relevant galaxies. A meaningful test also requires that the index profiles are at least tentatively detected: profiles that are consistent with being flat contain no information. In particular, we seek to match positive colour gradients (outskirts redder than the centre) to negative H δ_A gradients (outskirts older/more metal rich than the centre). For simplicity, we refer to both positive colour gradients and negative H δ_A gradients as inverse gradients, and vice versa, and negative colour gradients and positive H δ_A gradients are inside-out gradients.

Unfortunately, at the time of this writing, we can only present data for two galaxies (Fig. B1). The proposed approach is in fact limited by the unavailability of suitable data. As a precondition, we have reliable COSMOS F814W photometry for all the PSB galaxies in our sample, but, in general, suitable redder-wavelength images are unavailable. When available, these images have broader PSF than F814W photometry, and as a result, raw images show an artificially high fraction of galaxies with blue centres. Therefore, we also require a reliable PSF deconvolution, which further limits the sample size. The overlap with the CANDELS Survey is insufficient (Grogin et al. 2011): Out of 17 PSB galaxies considered here, only galaxy 211263 M1 is present in CANDELS. This galaxy (not pictured) has flat H δ_A profile and negative colour gradient, and is therefore uninformative.

The COSMOS-DASH Survey (hereafter, DASH; Mowla et al. 2019) provides *HST* F160W imaging of the COSMOS field. Given that LEGA-C is selected from the COSMOS field, and that DASH

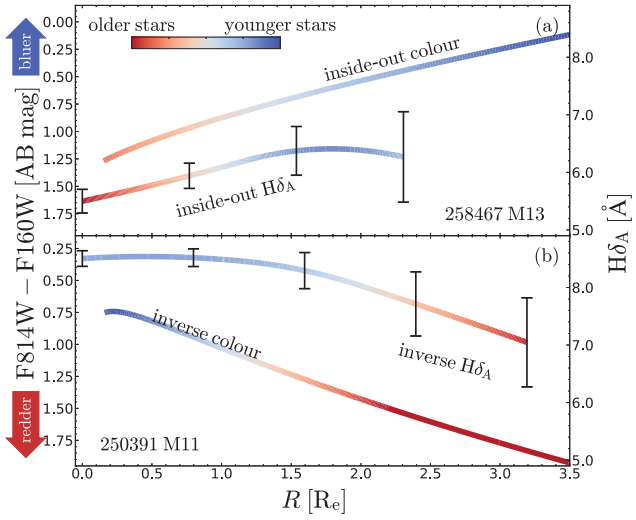

Figure B1. We show the clear connection between rest-frame optical colour profiles (lines with no error bars, left-hand scale) and H δ_A profiles (lines with error bars, right-hand scale), for the two PSB galaxies with both available colour profiles *and* significant H δ_A gradients. 258467 M13 shows clear inside-out structure (outskirts bluer and with stronger H δ_A than the centre; Panel B1a), whereas 250391 M11 shows clear inverse structure (outskirts redder and with weaker H δ_A than the centre; Panel B1b). The lines are arbitrarily colour coded so that bluer optical colour and stronger H δ_A absorption, corresponding to relatively younger stars, are rendered by bluer colour hues.

currently covers ≈30 per cent of this field, the DASH data are available for five of our PSB galaxies. Of these, one is galaxy 211263 M1, which we have already discarded. Of the remaining four galaxies, two more have flat H δ_A gradient (110805 M3 and 216730 M9); moreover, both of these galaxies have unreliable GALFIT fits, in that the best-fitting parameters reached the limits of the allowed range. The reason is probably that DASH is less deep than either COSMOS or CANDELS: the five σ point-source detection limit for DASH is $H = 25.2$ mag (Mowla et al. 2019), whereas CANDELS has $H = 27$ mag (Grogin et al. 2011) and COSMOS has $I = 27.2$ mag (Koekemoer et al. 2007). We are left with only two PSB galaxies. The first (258467 M13; Panel B1a) has both inside-out colour and inside-out H δ_A profile, whereas the second (250391 M11; Panel B1b) has both inverse colour and inverse H δ_A profile.

The agreement between the two reliable index gradients with the respective colour gradients is a reassuring consistency check for our methodology. We conclude that our detection of an inverse age gradient in the typical PSB is a robust result, and that space-based photometry may represent an alternative mean to investigate the inverse or inside-out structure of PSB galaxies.

This paper has been typeset from a TEX/LATEX file prepared by the author.